https://doi.org/10.5194/egusphere-2026-4536
Preprint. Discussion started: 24 August 2026

High-Resolution Boundary-Layer Detection Lidar for Spaceborne Applications: Parameter Design, Theoretical Simulation, and Airborne Validation

Kexin Ming[1,3], Chong Wang[1,6,] Wei Kong[5], Xianghui Xue[1,2,3,4], Genghua Huang[5], Ruikai Xue[5], Wenhao Li[1,3], Yudie Li[1,3], Chen Liang[3], Ruocan Zhao[1,3], Mingjiao Jia[7,8], Xiang Shang[7,8]

[1]School of Earth and Space Sciences, University of Science and Technology of China, Hefei 230026, China
[2] National Field Observation and Research Station (Anhui Mengcheng) for Geophysics, University of Science and Technology of China, Hefei 230026, China
[3]Hefei National Laboratory, University of Science and Technology of China, Hefei 230026, China
[4]Hefei National Research Center for Physical Sciences at the Microscale and School of Physical Sciences, University of Science and Technology of China, Hefei 230026, China
[5]Shanghai Institute of Technical Physics, Chinese Academy of Sciences, Shanghai 200083, China
[6]China Meteorological Administration Xiong'an Atmospheric Boundary Layer Key Laboratory, Xiong'an New Area, Hebei 070000, China
[7]Wuhan Institute of Quantum Technology, Wuhan 430000, China
[8]Shandong Guoyao Quantum Radar Technology Co., Ltd., Jinan 250000, China

Correspondence to: Chong Wang (wclhy50@ustc.edu.cn) and Wei Kong (kongwei@mail.sitp.ac.cn)

Abstract. The planetary boundary layer height (PBLH) is a key parameter for studying global land-atmosphere interactions, weather forecasting, and climate change. However, owing to the limited adaptability of existing detection techniques over complex terrain and the lack of observational consistency across different environments, unified and refined boundary layer observations on a global scale remain a major challenge. To support future spaceborne lidar missions for global boundary layer monitoring, this study establishes a closed-loop framework integrating spaceborne parameter design, theoretical simulation, and airborne experimental validation. As a core technical advance, a scaled airborne prototype was developed, and a synergistic terrain-atmosphere detection regime was introduced. By synchronously acquiring surface elevation and atmospheric backscatter signals, the system can directly retrieve the boundary layer height relative to the actual ground surface, namely above ground level (AGL), thereby fundamentally mitigating the terrain-matching bias of conventional approaches. System performance was primarily validated through the Yulin nighttime flight experiment, where the retrieved BLH showed a median difference of 10 m and a maximum RMSE of 45 m relative to the ground-based reference. The additional Hainan daytime flight experiment indicated the system's detection potential under strong background illumination and complex cloud conditions. This study validates the performance of the airborne prototype and provides empirical evidence for the parameter design of future spaceborne detection systems, supporting the construction of a globally consistent and high-precision boundary layer observation network.

https://doi.org/10.5194/egusphere-2026-4536
Preprint. Discussion started: 24 August 2026

1 Introduction

The planetary boundary layer, as the lowest layer of the atmosphere, connects the Earth's surface with the free atmosphere. It is strongly influenced by thermal and dynamic effects from the Earth's surface and serves as the atmospheric structure for the exchange of mass and energy between the atmosphere and the Earth's surface. It has profound impacts on human life and societal activities. In recent years, frequent major meteorological disasters, air pollution, and degradation of ecosystem functions around the world are critically tied to the evolution of boundary layer structure at the regional scale. Therefore, in-depth research into the spatiotemporal evolution of the atmospheric boundary layer structure and a deeper understanding of its thermodynamic and dynamic processes are crucial for advancing our knowledge of land-atmosphere interactions and atmospheric environmental evolution patterns. Furthermore, such research holds great scientific importance and considerable practical value in addressing precise weather forecasting, responding to climate change, and sustaining ecological health. The planetary boundary layer height (PBLH), as an important parameter characterizing the depth of the boundary layer, is also a key parameter in many land-atmosphere coupling indices. Accurate measurement of the PBLH is essential for deriving science-based emission management through inverse pollutant transport modeling (Wang et al., 2019). Additionally, the PBLH directly influences the thermal capacity of the boundary layer and plays a critical role in precipitation initiation. Moreover, as dominant constituents of the boundary layer, aerosols are directly linked to atmospheric chemistry, cloud formation, and climate change. Understanding the spatiotemporal patterns of aerosol variations can help us better comprehend their climate effects and formulate measures to control atmospheric pollution. In addition, a bidirectional coupling exists between aerosols and the PBLH, wherein the PBL governs aerosol transport and vertical mixing, while aerosol distribution modulates PBL development in turn (Liu et al., 2022). The construction and optimization of PBL structure and evolution patterns are critical for advancing weather and climate numerical models(Su and Zhang, 2024). Deviations in the parameterization of PBLH within models directly lead to uncertainty in wind field patterns and surface flux, constituting a primary source of error in the forecasting of pollutant dispersion and diverse meteorological phenomena. Hence, how to develop a PBL parameterization scheme with global complexity and diversity remains an urgent problem for weather forecasting and climate prediction. The main reason for this dilemma is the lack of globally consistent observational datasets on the PBLH (Wang et al., 2023).

As an active remote sensing instrument, lidar can obtain aerosol optical parameters and PBLH with high spatiotemporal resolution (Comerón et al., 2017; Cairo et al., 2024). On the basis of the observation platform, lidar can be divided into ground-based, airborne, and spaceborne systems. Ground-based lidar offers advantages such as low cost, easy maintenance, and the ability to provide long-term, stable observations at fixed location. Typical ground-based lidar systems include the European Aerosol Research Lidar Network (EARLINET) (Pappalardo et al., 2014), the Micro-Pulse Lidar Network (MPLNET) (Berkoff et al., 2003; Welton et al., 2021), and the Asian Dust and Aerosol Lidar Observation Network (AD-Net) (Sugimoto et al., 2016). Compared with ground-based lidar systems, airborne lidar systems enable observations over much broader spatial scales. Notable examples include the first- and second-generation Langley Airborne High Spectral Resolution Lidar (HSRL) developed by the National Aeronautics and Space Administration (NASA) (Hair et al., 2008; Burton et al., 2012; Sawamura

https://doi.org/10.5194/egusphere-2026-4536
Preprint. Discussion started: 24 August 2026

et al., 2017), and the airborne HSRL developed by the German Aerospace Center (DLR) for characterizing aerosol optical properties and types (Esselborn et al., 2009; Groß et al., 2013). However, airborne missions are limited by factors such as flight paths and meteorological conditions, making long-term observations and continuous data collection impossible. Spaceborne lidar can provide global observations of aerosol vertical profiles and PBLHs, exhibiting substantial potential for studying their continuous spatiotemporal variations and long-term statistical trends within specific regions. Since its launch in 2006, NASA's Cloud-Aerosol Lidar and Infrared Pathfinder Satellite Observation (CALIPSO) satellite has been thoroughly validated through comparisons with various ground-based detection data and airborne experimental data (Liu et al., 2015; Mason et al., 2024; Zhang et al., 2016). However, CALIPSO has inherent limitations; constraints in laser transmitter power, detector quantum efficiency, and integration time result in a low signal-to-noise ratio (SNR) during daytime. This makes accurate identification of the PBLH difficult by locating abrupt changes in aerosol concentration, thereby precluding an official CALIPSO BLH product (Liu et al., 2017). Additionally, due to instrument lifespan issues, CALIPSO concluded its detection mission in August 2023. To fill the potential observation gaps in the late stages of the CALIPSO mission and to validate next-generation high-resolution detection methodology, NASA deployed the Cloud-Aerosol Transport System (CATS) on the International Space Station (ISS) in 2015. As a technology demonstration, this mission marked a significant increase in spaceborne atmospheric remote sensing from high-pulse-energy linear mode to high-repetition-rate single-photon counting mode. CATS operated in orbit for approximately 33 months before its observations were concluded in October 2017 because of laser failure. Although CATS validated the feasibility of the single-photon counting methodology on a spaceborne platform, it still exhibited significant limitations in fine-scale detection of the PBL (Palm et al., 2021). On the one hand, CATS employs silicon avalanche photodiodes (Si-APD) as its detector in the 1064 nm band; limited by the physical properties of the material, its quantum efficiency in the near-infrared band is extremely low, typically only 3% to 5%, which severely constrains the ability to capture signals from large aerosol particles within the PBL. On the other hand, constrained by the low single-pulse energy design, the CATS observations during the day were highly susceptible to intense background solar radiation, making its data unsuitable for high-temporal-resolution retrieval of fine PBL structures during the day. Building on the validation of the CATS single-photon methodology (Pauly et al., 2019), spaceborne lidar technology has continued to evolve toward higher spectral resolution and independent retrieval capabilities. The most prominent example is the Earth Cloud Aerosol and Radiation Explorer (EarthCARE) satellite, which was jointly developed by the European Space Agency (ESA) and the Japan Aerospace Exploration Agency (JAXA) (Wehr et al., 2023). Successfully launched in May 2024, its atmospheric lidar, ATLID, is the first spaceborne instrument to utilize the 355 nm High-Spectral-Resolution Lidar (HSRL) technique, granting it the capability for independent extinction coefficient retrieval (do Carmo et al., 2021; Donovan et al., 2024). However, this system also faces inherent physical limitations for PBL detection: the ultraviolet band is affected by strong molecular Rayleigh scattering, where intense near-surface molecular background signals can easily mask weak PBL backscattering features. Furthermore, the 355 nm wavelength exhibits a weaker response to the large aerosol particles commonly found within the PBL. Therefore, although the EarthCARE mission has distinct advantages in high-precision observations of high-altitude aerosols and clouds (Mason et al., 2024), it still struggles to meet the requirements for fine-scale observations of the near-surface PBL. From CALIPSO and

CATS to EarthCARE, despite the continuous progress in spaceborne lidar technology, the challenge of achieving unified global observations of PBLH remains unresolved, leaving a gap in the field that urgently needs to be filled. Consequently, it is essential to develop a new high-resolution atmospheric boundary layer lidar payload. To this end, this study proposes a detection system that integrates atmospheric profile detection with high-precision terrain mapping. This system aims to achieve precise three-dimensional spatial alignment between fine atmospheric structures and surface topography. This enables the direct retrieval of high-accuracy above-ground-level PBLH over complex terrains and effectively overcomes the geometric biases inherent in traditional atmospheric lidar observation systems.

In the process of developing a high-resolution atmospheric boundary layer lidar payload, theoretical simulation and scaled prototype flight experiments are the two core elements that ensure the scientific validity and feasibility of parameter design (Ke et al., 2022). Theoretical simulations can predict detection performance under different weather conditions by constructing multi-dimensional coupled models such as laser atmospheric transmission models, aerosol scattering models and atmospheric models. It can verify the rationality of the parameter design from a physical principle perspective and lay a theoretical foundation for engineering implementation. Scaled prototype flight testing is a critical step in parameter validation. By constructing scaled prototypes and conducting actual detection in real flight environments, signal quality can be quantitatively evaluated, which not only facilitates corrections to theoretical models but also provides empirical support for parameter optimization and performance evaluation of the payload.

This study focuses on the theoretical verification and empirical support of the parameter design of spaceborne atmospheric boundary layer detection lidar. Section 2 introduces the core parameter design of spaceborne lidar and describes the construction of a simulation system based on theoretical models to simulate the detection performance of the spaceborne system from physical principles. Section 3 introduces the determination of equivalent parameters for the airborne-scale prototype and explains the ground testing data and flight experiment data. Section 4 provides a detailed analysis and interpretation of the flight experiment data, presents the results of a comparative analysis between the experimental observation data and the simulation data, and demonstrates the reliability and scientific validity of the experimental observation data. In section 5, the mutual verification conclusions of the theoretical simulation and airborne experiments are summarized, and the synergistic verification value of the two in the engineering design of spaceborne lidar is explained.

2 Parameter design and theoretical simulation

2.1 Simulation theory

The laser beam emitted by the lidar system undergoes atmospheric scattering during propagation, with scattered radiation dispersing omnidirectionally. Lidar systems typically detect only backscattering signals, which are used to infer the properties of scatterers (Measures, 1984; Weitkamp, 2005). When only single scattering is considered, the ground-based lidar equation can be expressed as Eq. (1):

https://doi.org/10.5194/egusphere-2026-4536
Preprint. Discussion started: 24 August 2026

$$N(\lambda,z)=N_0(\lambda_0)[\beta(\lambda,\lambda_0,z,\theta)\Delta z\cdot[\frac{A}{z^2}]O(z)\eta(\lambda,\lambda_0)e^{\int_0^z-\alpha(\lambda_0,\xi)d\xi}e^{\int_0^z-\alpha(\lambda,\xi)d\xi}+N_B \quad (1)$$

where, $N(\lambda,z)$ is the power of the backscattering signal with wavelength λ received by the lidar in the altitude range ($z-\Delta z/2$, $z+\Delta z/2$), $N_0(\lambda_0)$ represents the laser emission power, $\beta(\lambda,\lambda_0,z,\theta)$ is the backscattering coefficient, Δz denotes the altitude resolution, A is the telescope receiving area, $O(z)$ is the overlap factor, $\eta(\lambda)$ represents the efficiency of the lidar system, and $\alpha(\lambda_0,z)$ is the extinction coefficient of the laser emitted by the lidar system on the incident path. The expression $e^{-\int\alpha(\lambda 0,\xi)d\xi}$ represents the transmittance of the laser on the one-way path from the emission to the scatterer, $\alpha(\lambda,z)$ is the extinction coefficient of the scattered light after the interaction of the laser light with the scatterer, and $e^{-\int\alpha(\lambda,\xi)d\xi}$ represents the transmittance of the scattered light from the laser to the telescope along a single path after scattering by the scatterer (Fernald, 1984). N_B denotes the sky background light. With respect to the spaceborne lidar system, the path of the laser differs from that of the ground-based system (Ming et al., 2024). Considering only elastic scattering, rewriting the integration path of the above equation yields the theoretical expression for the photon counts of the backscattering signal in spaceborne lidar measurements at a specified wavelength, as given by Eq. (2):

$$N_{sig}(z)=N_0[\beta(z)\Delta z\cdot[\frac{A}{(z_{Sat}-z)^2}]O(z)\eta_{total}\,exp[-2\int_z^{z_{Sat}}\alpha(z')dz'] \quad (2)$$

where z_{Sat} is the satellite altitude; η_{total} represents the overall efficiency of the lidar system, which is the product of η_{tr} and the optical efficiency of the transmitter; η_{re} is the optical efficiency of the receiver; and η_{det} is the photon detection efficiency of the detector. These are the fundamental theoretical frameworks for simulating backscattering signals in high-resolution atmospheric boundary layer lidar systems.

2.2 System simulation parameters

Taking into account both the system's actual operating environment and observation requirements, the key parameters of the high-resolution atmospheric boundary layer lidar system have been provisionally determined, and simulations have been conducted accordingly. Table 1 lists the system parameters used for the simulation and includes the corresponding parameters of the CATS payload (Pauly et al., 2019)—which employs the same spaceborne single-photon detection regime—for comparison. Building upon existing mature designs, the proposed system's parameter design can achieve a significant enhancement in detection performance by further improving key indicators such as single-photon detection efficiency.

Table 1. Simulation parameters for the high-resolution atmospheric boundary layer lidar system

#	Parameter	Value	CATS/ISS
1	Laser wavelength	1064 nm	1064 nm
2	Single pulse energy	4 mJ	1 mJ

https://doi.org/10.5194/egusphere-2026-4536
Preprint. Discussion started: 24 August 2026

3	Repetition rate	1000 Hz	5000 Hz
4	Optical transmittance of the transmitting unit	90%	/
5	Optical transmittance of receiving unit	50%	/
6	Telescope diameter	0.6 m	0.6 m
7	View angle of receiving field	58 μrad	110 μrad
8	Filter bandwidth	≤0.3 nm	/
9	Detector type	InGaAs-APD	Si-APD
10	Photon detection efficiency of the detector	20%	2%
11	Orbit altitude	600 km	410 km

2.3 Atmospheric model

The detection performance of lidar is highly dependent on the physical properties of the atmospheric environment, especially in boundary layer detection, which is based on the theory of aerosol tracer effects. To describe the atmospheric environment as comprehensively and reasonably as possible, it is essential to construct differentiated models for weather conditions with significant differences in aerosol distribution (Su et al., 2020b). We selected three typical weather conditions, clear and cloudless, mild-haze, and dust events, and used ground-based lidar measurement data to construct a parameterized laser atmospheric back-attenuation model for each weather condition.

In clear and cloudless weather, the atmospheric environment is relatively clean, and atmospheric extinction is dominated mainly by Rayleigh scattering of air molecules and a small amount of Mie scattering of aerosol particles. The aerosol content is low at low altitudes, resulting in good overall visibility. The mathematical model of the parameterized aerosol extinction coefficient under clear and cloudless weather conditions is represented by the blue solid line in Fig. 1.

https://doi.org/10.5194/egusphere-2026-4536
Preprint. Discussion started: 24 August 2026

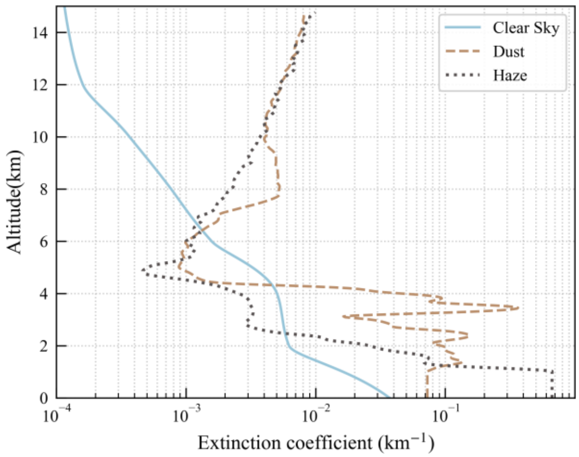

Figure 1. Aerosol extinction coefficient profiles under clear and cloudless, mild haze, and dust-event conditions. The blue solid, dark-gray dotted, and light-brown dash-dotted lines represent clear and cloudless weather, mild haze conditions, and dust-event conditions, respectively.

Under mild haze conditions, the concentration of PM2.5 in the atmosphere is significantly greater than that in clean atmospheric environments, generally ranging from 75 to 115 μg/m³. The aerosols in the boundary layer are mainly fine particles such as sulfates, nitrates, and organic carbon (Gao et al., 2021; Huang et al., 2014). The corresponding mathematical model of the parameterized aerosol extinction coefficient is shown by the dark-gray dotted line in Fig. 1.

During a dust event, particles suspended in the air exhibit a distinct stratification phenomenon. Larger dust particles, owing to their greater mass, predominantly accumulate within the lower atmosphere at altitudes of tens to hundreds of meters above ground level. In addition to surface winds, they undergo turbulent rolling and dispersion, forming a distinct turbid air layer near the surface (Tang et al., 2020; Tao et al., 2021). Finer particles are entrained upward by atmospheric currents to higher altitudes, generating spatially extensive suspended layers. As shown in Fig. 1, the light-brown dash-dotted line represents the mathematical model of the parameterized aerosol extinction coefficient under dust-event conditions.

2.4 Noise model

To further evaluate the detection performance of the lidar system, simulating the SNR parameter is indispensable; thus, establishing an accurate noise model is crucial. For lidar systems, noise can be divided into external and internal noise according to its source. The external noise is mainly sky background noise, whereas the internal noise is mainly dark counts of the detector (Degnan, 2002; Marais et al., 2016; Weitkamp, 2005). From the system itself, the background photon counts corresponding to each pulse and each distance gate are as follows:

$$N_{back} = [\eta_{re}\eta_{det} \times A_{tel} \times \frac{\pi\theta_{re}^2}{4} \times \frac{S_{TOA,up}}{hc/\lambda} \times \Delta\lambda + N_{dark}] \times \frac{2\Delta z}{c} \quad (3)$$

https://doi.org/10.5194/egusphere-2026-4536
Preprint. Discussion started: 24 August 2026

where η_{re} is the optical efficiency of the receiver and η_{det} is the photon detection efficiency of the detector. θ_{re} is the viewing angle of the telescope, $S_{TOA,up}$ is the top-of-atmosphere radiance at a specified wavelength, $\Delta\lambda$ is the filter bandwidth, and N_{dark} is the dark count rate. Given that all the parameters of the lidar system are determined, the only unknown quantity is the top-of-atmosphere radiance. By conducting a reasonable and accurate assessment of this parameter, an accurate noise mathematical model can be obtained. The curve of the background photon count rate with respect to the top-of-atmosphere spectral radiance is shown in Fig. 2.

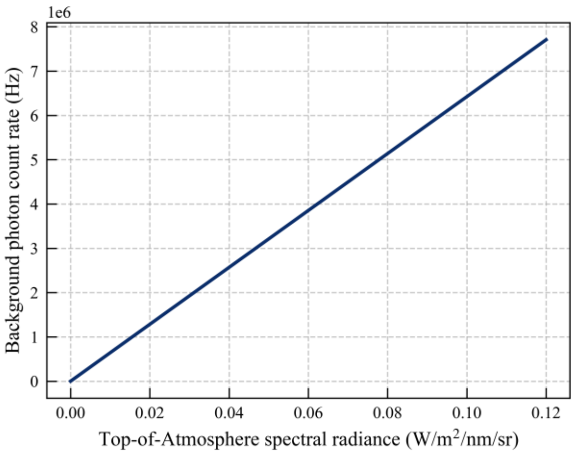

Figure 2. Background photon count rate versus top-of-atmosphere spectral radiance at 1064 nm.

MODTRAN, an atmospheric radiation transfer simulation software developed by the U.S. Air Force Research Laboratory, models the radiation transfer process in the atmosphere and quantifies the top-of-atmosphere radiance (Acharya et al., 1999; Berk et al., 1998, 2005). On the basis of the orbital and pointing parameters of the satellite during post-deployment observation operations, all necessary parameters in MODTRAN are configured. Considering that spaceborne lidar systems survey extensive areas during operational missions, covering diverse surface types, the surface albedo was varied from 0.1 to 0.6 to represent typical backgrounds such as paved surfaces, vegetation, dry soil, and moist soil (Gao et al., 2005; Jin et al., 2003). The detailed MODTRAN simulation results for the six albedo values are provided in Appendix A. As shown in Fig. 3 below, the simulated radiance results indicate a 1064 nm band radiance of 0.002–0.012 W/m²/nm/sr. This corresponds to a background photon count rate of 125–750 kHz received by the system.

https://doi.org/10.5194/egusphere-2026-4536
Preprint. Discussion started: 24 August 2026

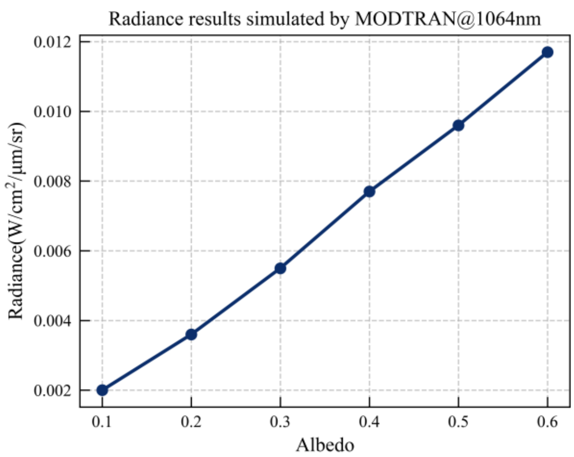

Figure 3. MODTRAN-simulated radiance at 1064 nm under different surface albedo values. The points represent the extracted radiance values at 1064 nm, and the line is added to show the trend with increasing albedo.

To enhance the credibility of noise assessment, we utilize measurement data from the low-light-level medium-resolution spectral imager (MERSI-LL) aboard the FY-3E satellite, which operates in a sun-synchronous near-polar orbit, for background noise evaluation (Shao et al., 2022; Zhang et al., 2024). MERSI-LL is a visible/infrared radiometer with low-light imaging capability. Among its observational channels, Channel 1 is a low-light channel with a 400 nm broadband, enabling high-dynamic-range observations near the terminator through three-gain settings (Wen et al., 2025; Yu et al., 2023). We utilize Channel 1 data to evaluate the top-of-atmosphere radiance. For a comprehensive assessment across seasons, one day of observational data was selected from each season. The MERSI-LL channel information and the distributions of the selected daily observations are provided in Appendix B.

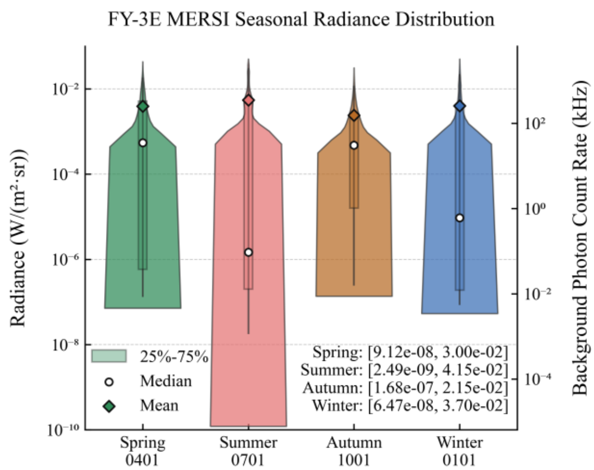

Figure 4. Seasonal distributions of equivalent 1064 nm in-band background radiance derived from MERSI-LL Channel 1 observations. The right axis indicates the corresponding background photon count rate.

https://doi.org/10.5194/egusphere-2026-4536
Preprint. Discussion started: 24 August 2026

Because MERSI-LL Channel 1 provides broadband radiance measurements over a bandwidth of 400 nm, the observations cannot be directly used as the in-band background radiance of the 1064 nm lidar system. Although the spectral radiance within this broadband range is not uniformly distributed with wavelength, it can be approximated as uniform for an order-of-magnitude assessment of the background photon count rate. On this basis, the Channel 1 measurements were converted into equivalent in-band radiance values by scaling them according to the 0.3 nm filter bandwidth of the lidar system. Figure 4 shows the seasonal distributions of the converted equivalent radiance values and the corresponding background photon count rates. After excluding outliers, the equivalent background radiance derived from the measurements remains below 0.04 W/m²/Sr, corresponding to a background photon count rate of less than 250 kHz. This observational estimate is consistent with the radiance range obtained from the MODTRAN simulations and was therefore used as a conservative background noise level in the subsequent theoretical simulations.

2.5 Theoretical simulation

Following the establishment of the theoretical models, the detection performance of the spaceborne lidar system was simulated. As shown in Fig. 5, the backscattering signal profiles are presented for three typical weather scenarios: clear and cloudless weather, mild haze, and dust events. The simulations were conducted with a background photon count rate of 250 kHz, a system vertical resolution of 30 m, and along-track horizontal resolutions exceeding 2 and 4 km, respectively.

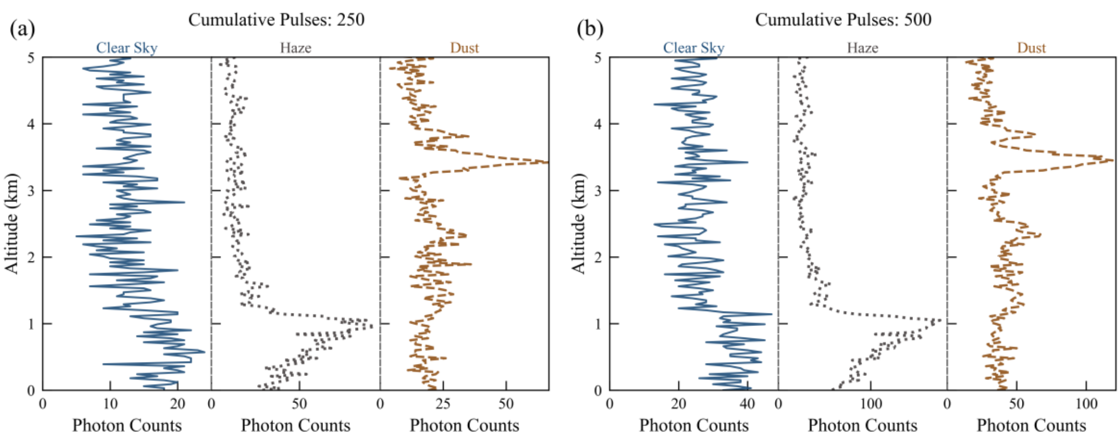

Figure 5. Simulated backscattering signal profiles under three typical weather conditions with accumulated pulse numbers of (a) 250 and (b) 500. The profiles are horizontally shifted within each subplot for clarity.

Here, Fig. 5a represents the case with an accumulated pulse count of 250, corresponding to a temporal resolution of 0.25 s and an along-track detection resolution exceeding 2 km. Similarly, Fig. 5b represents the case in which the along-track resolution exceeds 4 km. To facilitate visual comparison, the profiles under different weather scenarios are horizontally shifted within each subplot. The comparison reveals distinct backscattering signal profiles under different weather conditions in the simulations. During mild haze and dust events, aerosol layers exhibit more pronounced distribution characteristics, resulting in more significant features in the corresponding backscattering signals.

https://doi.org/10.5194/egusphere-2026-4536
Preprint. Discussion started: 24 August 2026

3 Ground and flight tests

3.1 System design

By integrating the theoretical simulation results with practical application scenarios, we designed the lidar system structure illustrated in Fig. 6a.

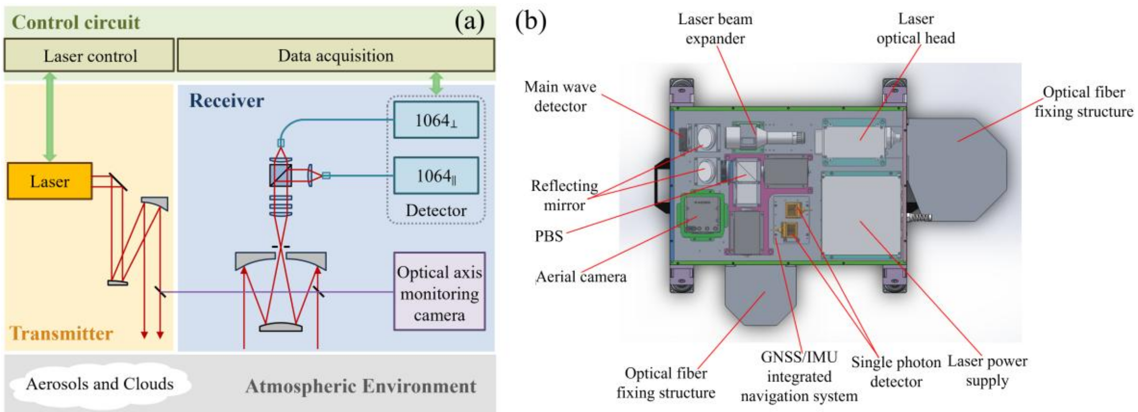

Figure 6. (a) Schematic diagram of the spaceborne lidar system design. (b) Structural schematic illustration of the airborne lidar prototype.

The system comprises five primary modules: laser transmission, backscattering signal reception, signal detection, boresight monitoring, and thermal control. Specifically, the laser transmission module integrates a laser source and beam expander; the backscattering signal reception module consists of a receiving telescope and post-optical path components; the signal detection module incorporates SPAD and data acquisition circuits; and the boresight monitoring module employs a boresight camera and piezoelectric steering mirror.

To simulate and replicate detection signals from the atmospheric boundary layer lidar payload operating at orbital altitudes of several hundred kilometers within the Earth's atmosphere, equivalent parameters for the airborne prototype were determined on the basis of theoretical models using signal intensity as the benchmark. Table 2 compares the equivalent parameters between the spaceborne lidar system and airborne-scale prototype, quantitatively validating the equivalence criteria followed in the scaled design (Paffrath et al., 2009; Reitebuch et al., 2009). Different filter bandwidths were used in the two flight experiments to meet their respective background-noise scaling requirements. A 0.3 nm filter was used during the Yulin nighttime experiment. During the Hainan daytime experiment, a 2.4 nm filter was deliberately used to increase the collected solar background and bring the background-noise scaling parameter of the airborne receiver closer to that of the spaceborne system under daytime conditions. These findings demonstrate that flight test data from the airborne prototype can replicate the detection characteristics of the spaceborne system in terms of signal features.

Table 2. Comparison of equivalent parameters between the spaceborne lidar system and airborne-scale prototype

#	Parameter	Spaceborne system	Airborne system

https://doi.org/10.5194/egusphere-2026-4536
Preprint. Discussion started: 24 August 2026

1	Laser wavelength	1064nm	1064 nm
2	Single pulse energy	≥ 4 mJ	1.1 mJ (Yulin) 0.4 mJ (Hainan)
3	Repetition rate	1000 Hz	2000 Hz
4	Pulse width	≤ 10 ns	≤ 10 ns
5	Laser divergence angle	≤ 30 μrad	≤ 200 μrad
6	Telescope diameter	600 mm	22 mm
7	View angle of receiving field	58 μrad	500 μrad
8	Filter bandwidth	≤ 0.3 nm	0.3 nm (Yulin) 2.4 nm (Hainan)
9	Flight altitude	600 km	10 km (Yulin) 5.7 km (Hainan)
10	Backscattering signal parameter Laser energy × Receiver aperture^2 ÷ Distance^2	4	5.324 (Yulin) 5.959 (Hainan)
11	Background noise parameter Receiving aperture^2 × Receiving field^2 × Filter bandwidth	1(Night) 363.12(Day)	1 (Yulin) 290.4 (Hainan)
12	Equivalent signal strength	1	1.3 (Yulin) 1.5 (Hainan)
13	Equivalent noise strength	1	1 (Yulin) 0.8 (Hainan)

Based on the aforementioned parameter design and flight test requirements, the finalized scaled airborne lidar prototype system design and structural schematic are presented in Fig. 6, corresponding to the spaceborne system design and airborne prototype structure, respectively.

270 In addition to the lidar system components, the prototype is equipped with an aerial camera and a GNSS/inertial navigation system (GNSS/INS) to perform synchronized image acquisition and collect position and attitude data. The aerial camera model is Phase One iXM-RS150F with a 150-megapixel resolution (14204 × 14204 pixels), a 33.1° × 25.1° field of view (FOV), and a ground coverage of 5.9 km × 4.5 km at a 10 km altitude. The GNSS/INS unit (Trimble APX-15) provides high-precision

https://doi.org/10.5194/egusphere-2026-4536
Preprint. Discussion started: 24 August 2026

timing signals to synchronize data acquisition for both the camera and the lidar system while simultaneously recording georeferenced coordinates and attitude parameters.

3.2 Ground-based testing

After completing the setup and assembly of the airborne lidar prototype in the laboratory, ground-based testing was conducted to verify its operational functionality before the flight experiments. To confirm the operational status of the equipment after long-term storage and transportation, prior to the second flight experiment, we performed ground-based testing on the airborne prototype in Qionghai city, Hainan Province. The prototype conducted slant-path atmospheric detection at a 45° elevation angle. The backscattering signal profiles acquired under nighttime and daytime conditions during ground-based testing are shown in Fig. 7a and b, respectively. Since no high-altitude clouds were present during the testing period and there was no obvious effective signal above 4 km, only the profiles within the 0–4 km altitude range are displayed. The temporal resolution was 0.125 s, corresponding to 250 accumulated pulses, and the range resolution was 30 m. In the nighttime signal, aerosols and cloud structures within the near-surface boundary layer are clearly visible, with the boundary layer top at an altitude of approximately 1.2 km. In contrast, in the daytime signal, the perpendicular polarization channel (ch1) is weak, and the depolarization ratio is extremely low. This phenomenon is closely related to the high-humidity environment in the Hainan region and the light rain weather on the day of testing. Under such conditions, aerosol particles are mostly spherical, resulting in a significant decrease in the depolarization signal. Furthermore, the backscattering signal of the parallel polarization channel (ch2) during the daytime exhibits a smoothly decreasing linear trend within the near-surface range of approximately 1.5 km in altitude, without any obvious abrupt changes in stratification. This finding indicates that within this altitude range, the aerosol concentration changes smoothly with altitude, and the vertical distribution is relatively uniform. Under such conditions, identifying a clear boundary layer top interface is difficult (Li et al., 2017b).

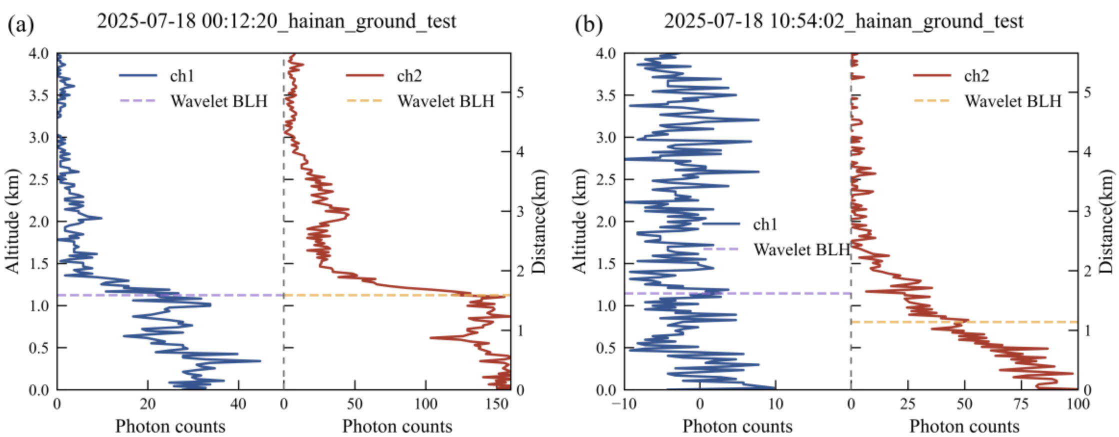

Figure 7. Measured backscattering signal profiles from ground-based tests in Qionghai city during (a) nighttime and (b) daytime.

https://doi.org/10.5194/egusphere-2026-4536
Preprint. Discussion started: 24 August 2026

3.3 Flight experiments

To evaluate the detection performance of the airborne prototype under the expected nighttime operating conditions and to further explore its performance under more complex daytime conditions, two flight experiments were conducted in Yulin, Shaanxi Province, in January 2025 and in Hainan Province in August 2025. The Yulin nighttime experiment was used as the primary validation under low-background-noise and stable-boundary-layer conditions, whereas the Hainan daytime experiment provided an additional evaluation under strong background noise and more complex atmospheric conditions. The former featured a simple structure and stable stratification, providing favorable conditions for evaluating the basic detection performance of the prototype. The latter was influenced by intense thermal convection, vigorous cumulus activity, sea–land breeze circulation, high humidity, and frequent cloud cover, resulting in rapid structural evolution and strong spatiotemporal heterogeneity. It therefore provided a challenging environment for exploring the daytime detection potential and limitations of the system. The geographical locations of the two experimental areas are shown in Fig. 9a.

In January 2025, we completed the first flight experiment in Yulin city, Shaanxi Province, China. Located in the northernmost part of Shaanxi, Yulin sits at the convergence of the Loess Plateau and the Mu Us Desert, forming a characteristic transitional zone with complex and diverse topography. The north predominantly features aeolian sand and grasslands, whereas the south consists of the loess hilly gully region. This region experiences a mid-temperate semiarid continental monsoon climate. The flight experiment was conducted during the winter season, characterized by a cold and dry climate, with average temperatures ranging from -10 °C to -5 °C, and frequent, strong northwesterly winds, resulting in severe environmental conditions. Under winter nighttime and early morning conditions, surface radiative cooling favors the formation of a stable boundary layer, while the weak solar radiation before sunrise corresponds to a relatively low background noise level. Consequently, the early morning boundary layer typically remains shallow and stable, providing an ideal observational case for evaluating the prototype under weak-noise and stable-boundary-layer conditions.

In August 2025, we conducted a second flight experiment in Hainan Province. The experimental area was located in the southwestern coastal region of the island, backed by the spurs of the Limu Mountains—part of the central mountain range—and facing the vast Beibu Gulf. Situated at the northern margin of the tropics, Hainan experiences a tropical monsoon climate. The experiment was conducted during the summer, characterized by high temperatures, high humidity, and dramatic weather changes. Driven by intense solar radiation, the sea-land breeze effect, and active convective activities after sunrise, the boundary layer develops vigorously and exhibits rapid evolution and spatial inhomogeneity. Frequent low clouds, high humidity, and turbulent mixing further increase the complexity of signal extraction and boundary layer height retrieval. This environment provided a challenging scenario for evaluating the daytime detection performance of the airborne prototype under conditions of high humidity and strong convection.

A Cessna Citation S/II aircraft was utilized for both flight experiments. The scaled airborne lidar prototype was installed within the aircraft's pressurized cabin, and observations were conducted through an optical window. The aircraft and the installation setup of the prototype are shown in Fig. 8 below.

https://doi.org/10.5194/egusphere-2026-4536
Preprint. Discussion started: 24 August 2026

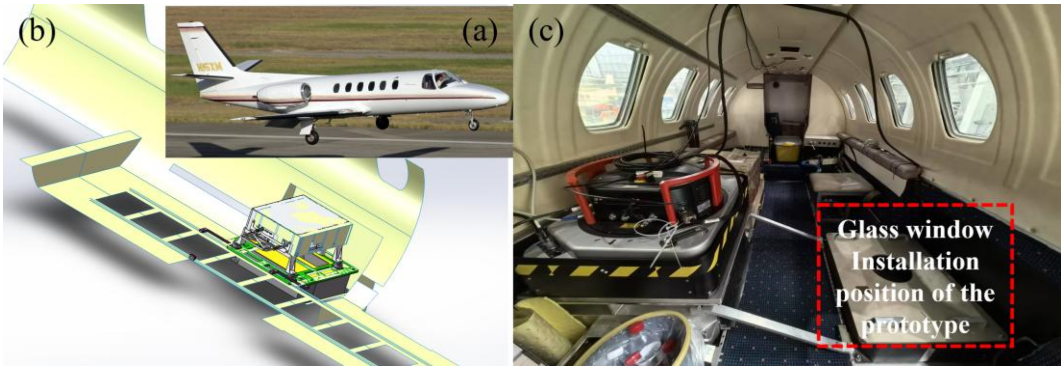

Figure 8. (a) Experimental aircraft. (b) Schematic illustration of the loading structure of the airborne prototype. (c) Actual photos taken inside the experimental aircraft. The red box indicates the position of the optical window on the aircraft, which is the installation location of the prototype.

Taking comprehensively into account factors such as weather conditions and airport scheduling, the final executed flight plan in Yulin, Shaanxi, commenced with a takeoff at approximately 06:30 local time (LT). This was followed by a 30-minute climb to the target altitude of 10 km. The aircraft subsequently cruised back and forth at a constant speed along a preset route, passing over the ground stations multiple times until it began a gradual descent after 08:20 LT to conclude the experiment. Given that the local sunrise on the day of the experiment occurred at 07:55 LT, the observational period was primarily during the nighttime. The planned flight route and the locations of the ground stations are illustrated in Fig. 9b.

In Hainan, owing to airspace control restrictions, the flight route could not be planned in advance. Consequently, the actual executed flight plan involved departing from Qionghai Bo'ao Airport at 07:30 LT, gradually climbing, and heading toward Dongfang city. There, the aircraft maintained a holding pattern at an altitude of 5.7 km until its descent began after 08:20 to end the experiment. The specific flight trajectory is depicted in Fig. 9c. Notably, local sunrise in Hainan occurred at 06:22 LT; thus, the entire experimental period occurred during the day. Furthermore, because the aircraft could not reach the planned altitude of 10 km owing to airspace restrictions, the laser pulse energy was reduced according to the actual flight altitude of 5.7 km to preserve the scaled signal strength. Meanwhile, a 2.4 nm filter was used instead of the 0.3 nm filter to increase the collected solar background and reproduce an approximately equivalent daytime background-noise condition.

https://doi.org/10.5194/egusphere-2026-4536
Preprint. Discussion started: 24 August 2026

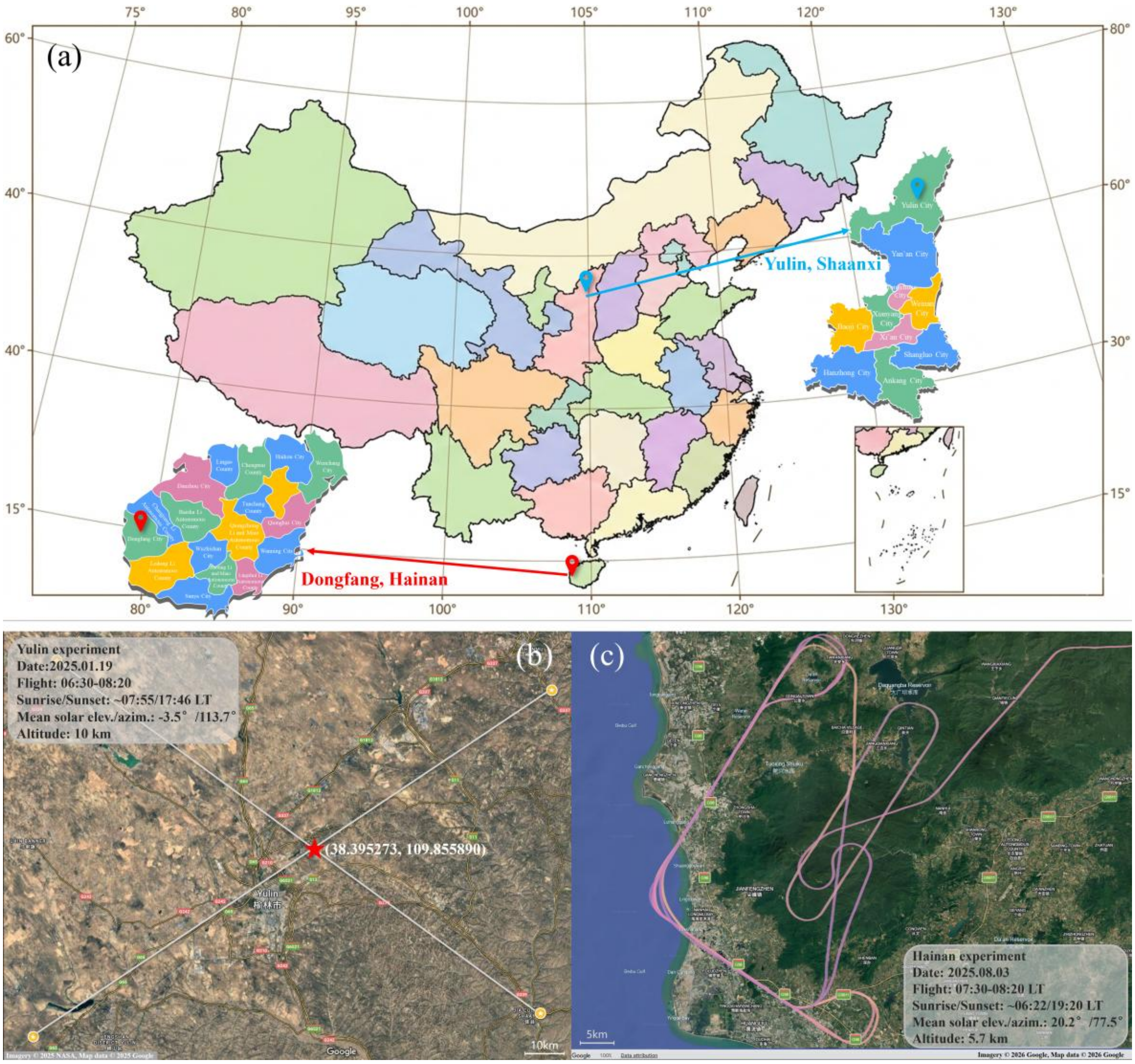

Figure 9. (a) Geographical locations of the two experimental areas, where the blue and red markers indicate Yulin city, Shaanxi Province, and Dongfang city, Hainan Province, respectively. The administrative boundaries were drawn by the authors using data obtained from the National Catalogue Service for Geographic Information of China, and the administrative-division information was checked against the information published by the Ministry of Civil Affairs of the People's Republic of China in 2025. (b) Schematic of the planned flight route for the Yulin experiment, with the solid grayish-white line representing the designed flight path. (c) Schematic of the flight trajectory for the Hainan experiment. The satellite imagery used as the base maps in (b) and (c) was obtained from Google Maps and Google Earth, respectively, with the corresponding copyright statements retained within each panel: (b) Imagery © 2025 NASA, Map data © 2025 Google; (c) Imagery © 2026 Google, Map data © 2026 Google.

The algorithm flowchart for the flight experiment data processing is shown in Fig. 10 below. Initially, low-quality data are filtered out from the raw lidar data collected during the flight experiments. Afterward, photon time-tagging and flight distance calculations are performed to obtain the photon point cloud data, as shown in Fig. 11a. Following range binning and pulse integration, backscattering signal profile data with a vertical resolution of 30 m and a temporal resolution of 0.125 s are obtained, as shown in Fig. 11b. Next, on the basis of the characteristics of a significant localized increase in signal intensity

https://doi.org/10.5194/egusphere-2026-4536
Preprint. Discussion started: 24 August 2026

caused by hard target reflection from the ground, terrain identification and surface alignment are conducted. Background noise is subsequently estimated and subtracted from the processed profile data, followed by a smoothing process. This yields spatiotemporally continuous backscattering signals referenced to the ground at 0 km (i.e., above ground level, or AGL), as shown in Fig. 11c. Specifically, the estimated background noise values can be extracted during the noise subtraction step, as depicted in the flowchart. Finally, on the basis of the variation characteristics of the backscattering signals at the top of the atmospheric boundary layer, the wavelet transform method is employed to identify the boundary layer top (Brooks, 2003), thereby deriving a time-varying sequence of boundary layer heights along the flight path. Because this study focuses on evaluating the system parameter design rather than developing an optimized BLH retrieval algorithm, the same traditional wavelet transform was consistently applied to both the Yulin and Hainan datasets as a baseline retrieval method.

https://doi.org/10.5194/egusphere-2026-4536
Preprint. Discussion started: 24 August 2026

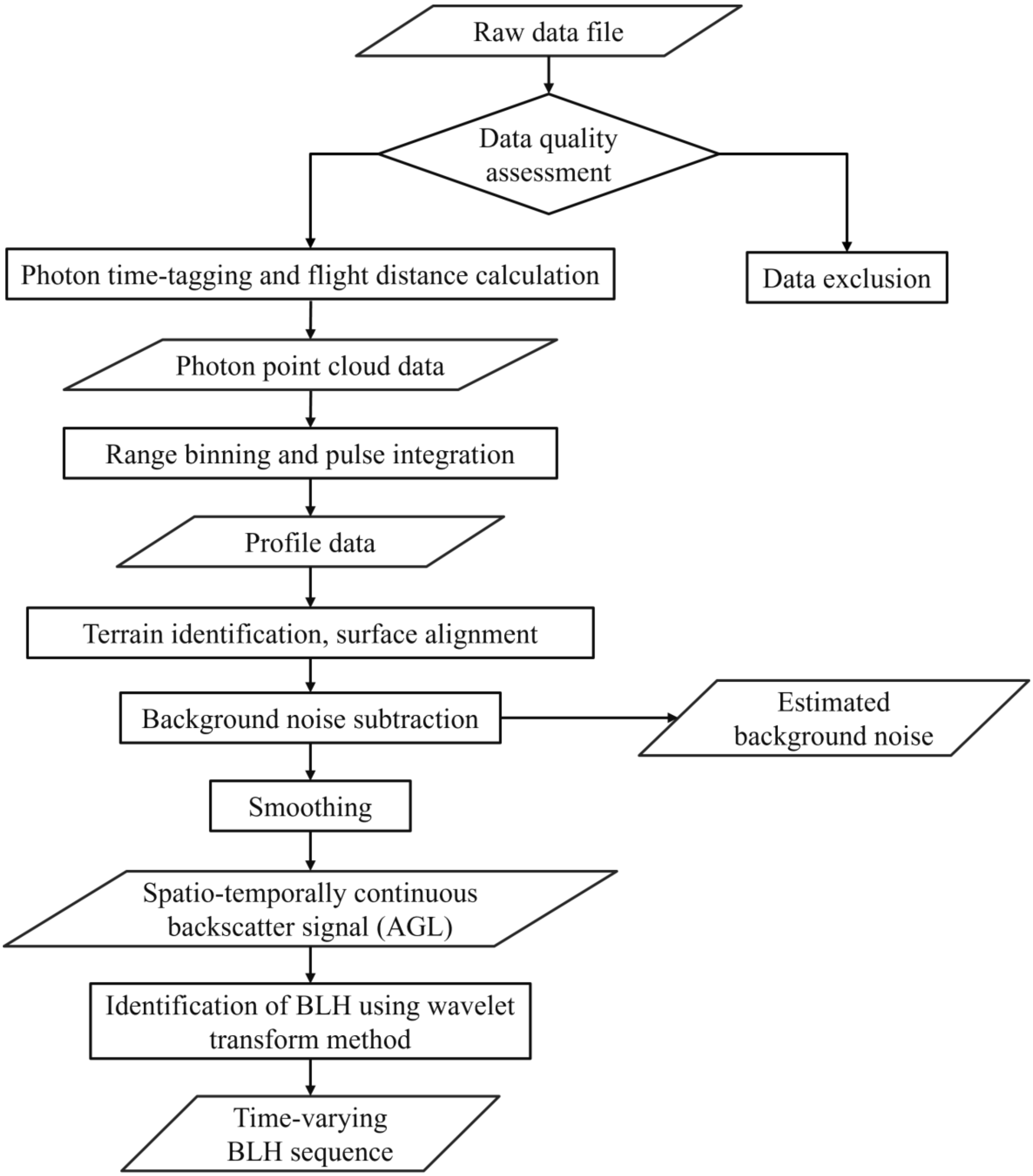

Figure 10. Flowchart of the flight experiment data processing

https://doi.org/10.5194/egusphere-2026-4536
Preprint. Discussion started: 24 August 2026

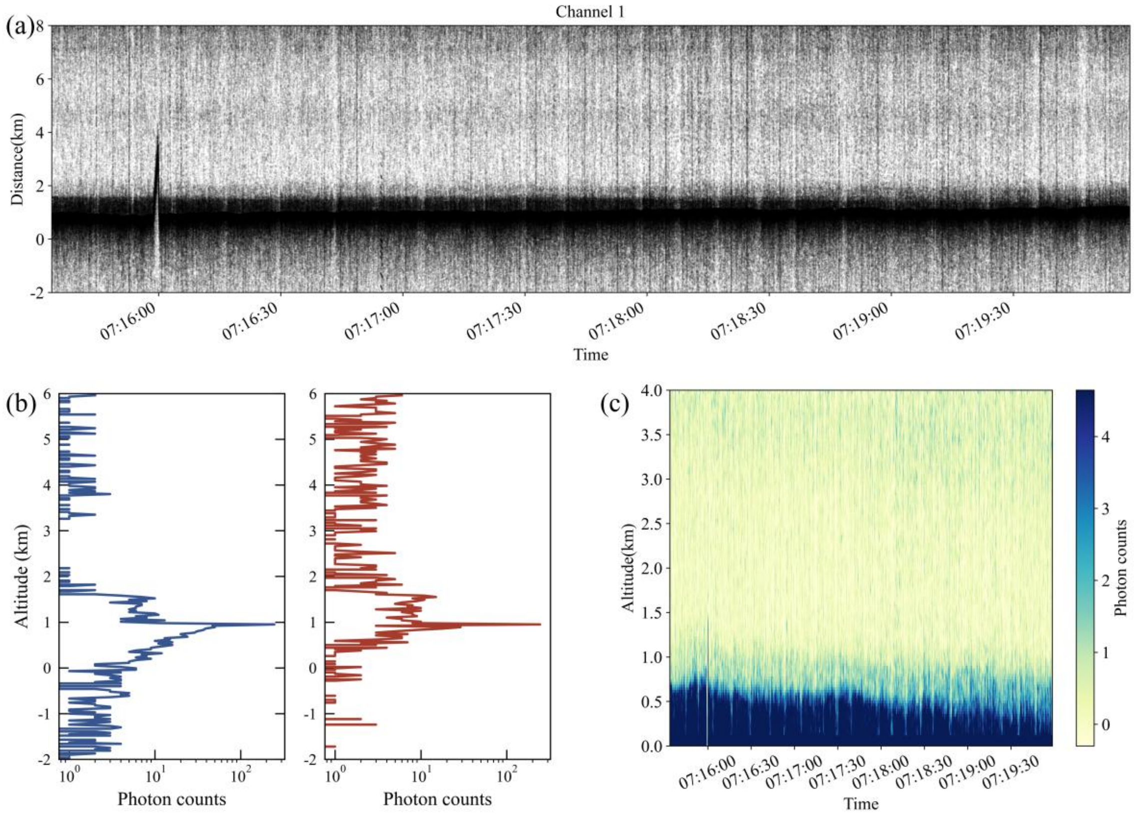

Figure 11. (a) Point cloud data. (b) Backscattering signal profiles with a vertical resolution of 30 m and a temporal resolution of 0.125 s. (c) Spatiotemporally continuous backscattering signals with the ground level normalized to 0 km.

Given that this flight experiment focuses primarily on the atmospheric boundary layer structure, data processing after background noise deduction was confined to the 0–4 km range to reduce the computational load and minimize unnecessary time complexity.

4 Results and discussion

To provide an intuitive and scientifically robust prelaunch assessment of the detection capability for the PBL by our designed spaceborne lidar system, we first generated a large ensemble of simulated signal profiles. This was accomplished by randomly generating numerous realizations of the theoretically calculated single-pulse backscattering profile according to a Poisson distribution. These profiles were then averaged according to the accumulated pulse count to simulate along-track detection scenarios. Finally, the wavelet covariance transform method was applied to this ensemble to identify the boundary layer top, yielding the derived boundary layer height sequences under the different weather conditions shown in Fig. 12 below.

https://doi.org/10.5194/egusphere-2026-4536
Preprint. Discussion started: 24 August 2026

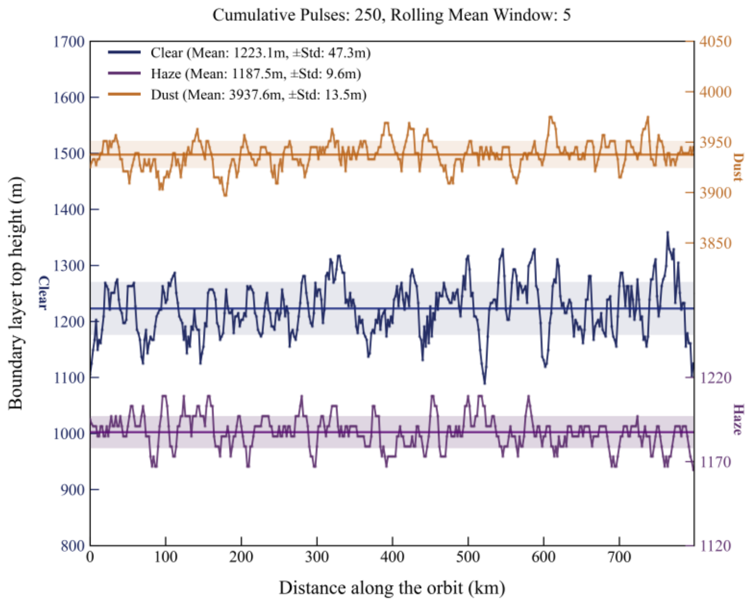

Figure 12. Theoretical simulation of the boundary layer top detection performance of the spaceborne lidar system under clear and cloudless weather, mild haze weather and dust event conditions. The deep navy blue, deep violet, and ochre brown points represent clear and cloudless weather, mild haze weather, and dust-event conditions, respectively.

The boundary layer top detection results under the three weather conditions are shown together in Fig. 12, with different colors representing different weather scenarios. Given that the atmospheric model for each weather condition is fixed, the boundary layer top height can be considered constant under each specific condition. Therefore, for a single weather scenario, it is reasonable to regard the mean value of the boundary layer top heights identified from the large ensemble of simulated profiles as the true value for that specific condition. In this context, the standard deviation of the identified boundary layer top height sequence represents the detection error of the spaceborne lidar system, thereby reflecting its detection accuracy for the boundary layer top. Under cloud-free conditions, both mild haze events and dust events clearly exhibit distinct aerosol layer distribution characteristics. Boundary layer top detection, which uses the aerosol tracer method, achieves higher precision under these conditions. Under all three weather scenarios, the theoretically simulated detection accuracy of the spaceborne lidar system for the boundary layer top is better than 10%.

To further evaluate the detection performance of the scaled airborne lidar prototype during the flight experiments, the results from both the Yulin and Hainan flight experiments were first compared with those of the theoretical simulation model. The estimated background noise during the nighttime period in Yulin and the daytime period in Hainan are presented in Fig. 13a. In terms of magnitude, the estimated background noise derived from the measured flight data remained on the order of kHz during the Yulin nighttime period. During the Hainan daytime observations, the background noise remained on the order of 10^2 kHz, which was comparable in magnitude to the daytime background considered in the theoretical simulations, supporting the validity of the background-noise scaling strategy. However, under conditions of dense cloud cover and strong solar reflection, the background noise even reached the 10^3 kHz level. This substantial increase was mainly related to the enhanced

https://doi.org/10.5194/egusphere-2026-4536
Preprint. Discussion started: 24 August 2026

reflection of solar radiation by clouds, which increased the background radiance entering the receiving field of view and consequently increased the background photon counts detected by the system. Therefore, the Hainan experiment included not only the expected daytime background-noise condition but also strongly reflecting cloudy conditions with background-noise levels exceeding the nominal simulation case. These observations provide further information for evaluating the daytime detection performance and its limitations under different cloud conditions.

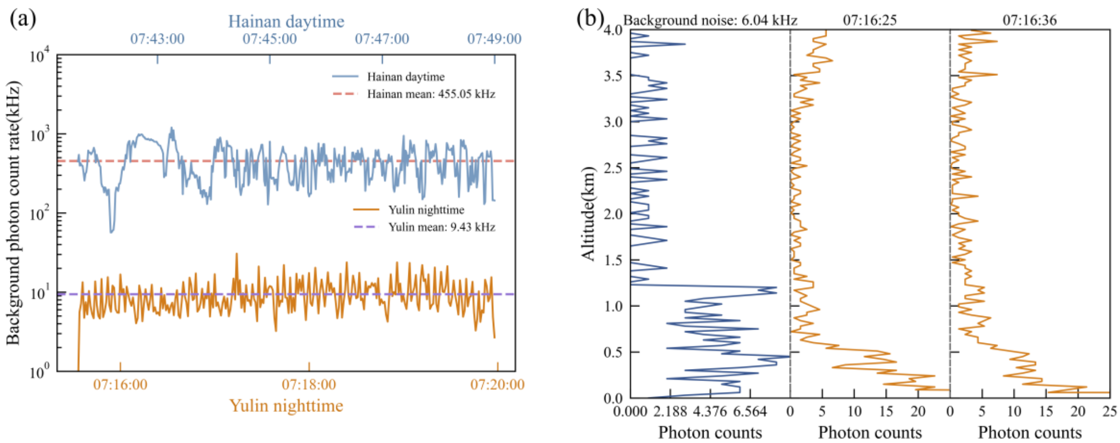

Figure 13. Comparison of theoretical simulations and measured flight data. (a) Estimated background noise during the Yulin nighttime and Hainan daytime flight experiments. (b) Comparison of theoretical simulation profiles and measured airborne profiles from the Yulin nighttime flight experiment.

Taking the Yulin nighttime flight experiment as an example, as observed from the backscattering signal profiles in Fig. 13b under comparable background photon count rates, a uniform vertical resolution of 30 m, and 250 accumulated pulses, the theoretically simulated signal profiles exhibit similar orders of magnitude in terms of photon counts and consistent overall variation trends compared with the measured flight data. This further confirms the scientific validity of the theoretical simulation model and demonstrates the superior detection performance of the airborne prototype.

To comprehensively evaluate the detection performance of the airborne lidar prototype and investigate its detection limits, the results from the two flight experiments are analyzed in detail separately.

4.1 Stable boundary layer during winter nighttime in Northwest China

From the data acquired during the Yulin flight experiment, the low and stable structural characteristics of the boundary layer during the winter nighttime in Northwest China can be clearly observed. As shown in Fig. 14a and b, two typical backscattering signal profiles, acquired along a single flight path with a temporal resolution of 0.125 s and a vertical resolution of 30 m, correspond to 07:26:04 LT and 07:40:41 LT, respectively. Both profiles indicate that aerosols are primarily concentrated within 1 km above the ground, which is consistent with the deep inversion layer structure typical of winter nights. Compared with the first profile, the second profile exhibits a more pronounced signal-gradient variation near 0.6 km, which may be related to local differences along the flight path and the continued influence of the stable nocturnal inversion before sunrise.

https://doi.org/10.5194/egusphere-2026-4536
Preprint. Discussion started: 24 August 2026

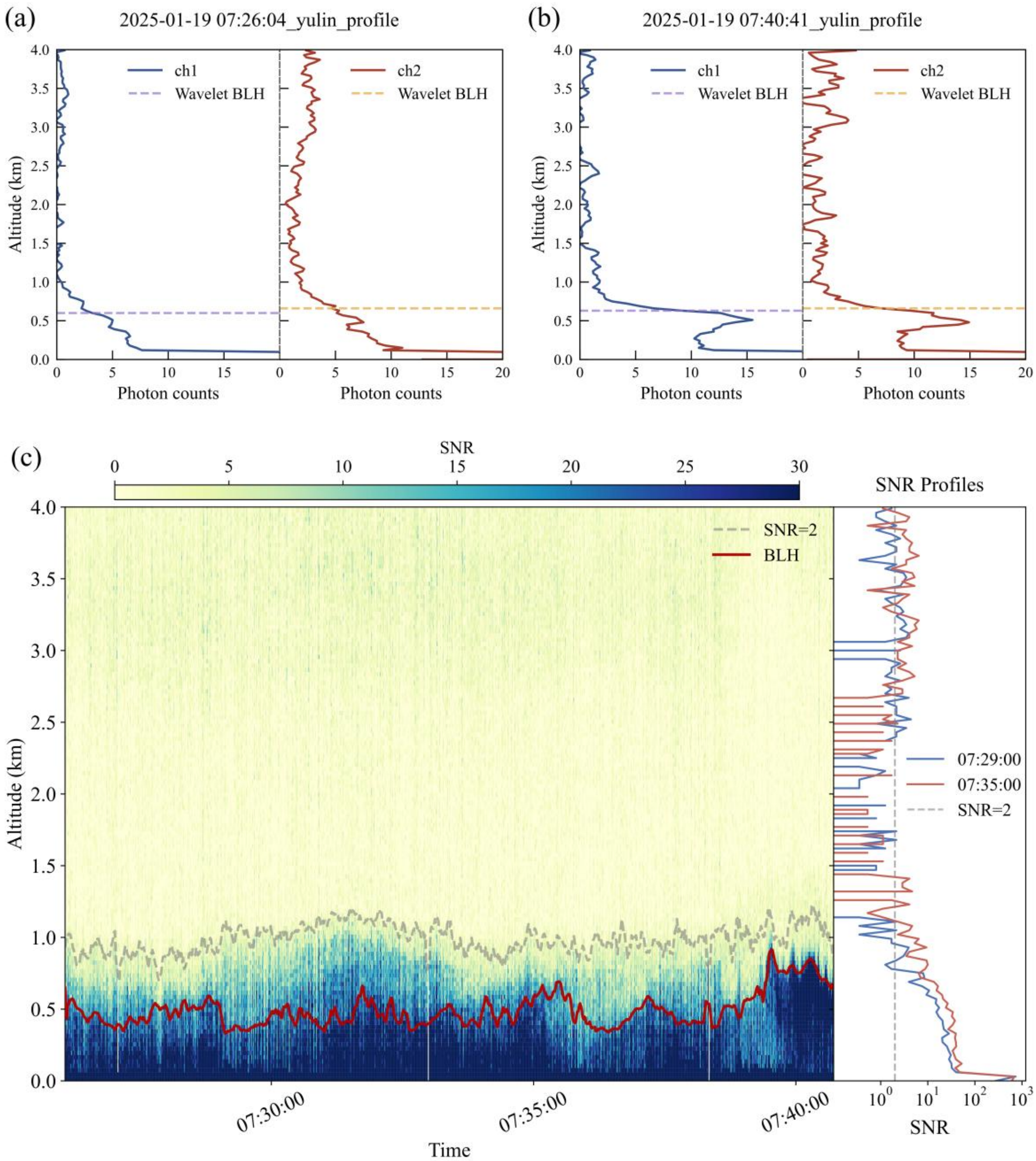

Figure 14. Airborne lidar observations of the stable boundary layer during the Yulin nighttime flight experiment. (a, b) Representative backscattering signal profiles at 07:26:04 and 07:40:41 LT, respectively, with dashed lines indicating the BLHs identified by the wavelet transform method. (c) Time-height distribution of the SNR, with the retrieved BLH sequence overlaid; representative SNR profiles are shown on the right.

Although the morphological features of the profiles at the two specific times differ, the BLHs retrieved using the traditional wavelet transform method are both approximately 0.6 km. This finding indicates that the position of the boundary layer top remains stable at the macroscopic level. To further examine the continuity of the retrieved boundary layer structure and the

https://doi.org/10.5194/egusphere-2026-4536
Preprint. Discussion started: 24 August 2026

signal quality during the corresponding flight period, the SNR time-height distribution is shown in Fig. 14c, with the time-varying BLH sequence overlaid. The results show that the BLH remains stable within a low range of 0.4–0.6 km, with minor fluctuations throughout most of the flight. This further corroborates the typical low and persistent characteristics of the stable boundary layer during winter nights in Northwest China.

Meanwhile, within an altitude range of 1 km AGL, the SNR consistently remains above 2, indicating that the airborne lidar system can effectively detect near-surface atmospheric structures. Conversely, the SNR decreases significantly within the 1–4 km altitude range. This is mainly because the stable inversion layer during winter nighttime suppresses the vertical diffusion of aerosols, confining them to the near-surface region and leaving the atmosphere above the boundary layer relatively clean (Li et al., 2022a; Prasad et al., 2022). As a result, the backscattering signal attenuates rapidly above the boundary layer, accompanied by a decrease in the SNR. These observational results are consistent with the optical properties of clean continental air masses in the free atmosphere, which further confirms the reliability of the observation data.

To ensure a comprehensive and rigorous validation of the absolute detection performance of the airborne lidar prototype, cross-validation is conducted using a ground-based 1550 nm lidar deployed directly beneath the flight path (Li et al., 2022b). A spatial matching grid of 2 km × 2 km centered on the ground station was constructed. Through a refined screening of the flight trajectory data, two overpass windows were identified: 07:33:08–07:33:19 and 07:37:12–07:37:34 LT. The continuous observation results from the ground-based 1550 nm lidar (vertical resolution: 30 m; temporal resolution: 1 min) during the experimental period are shown in Fig. 15a. The boundary layer top was retrieved using the identical wavelet transform method. The retrieved BLH from the ground-based lidar during the overpass periods was consistently determined to be 0.54 km.

https://doi.org/10.5194/egusphere-2026-4536
Preprint. Discussion started: 24 August 2026

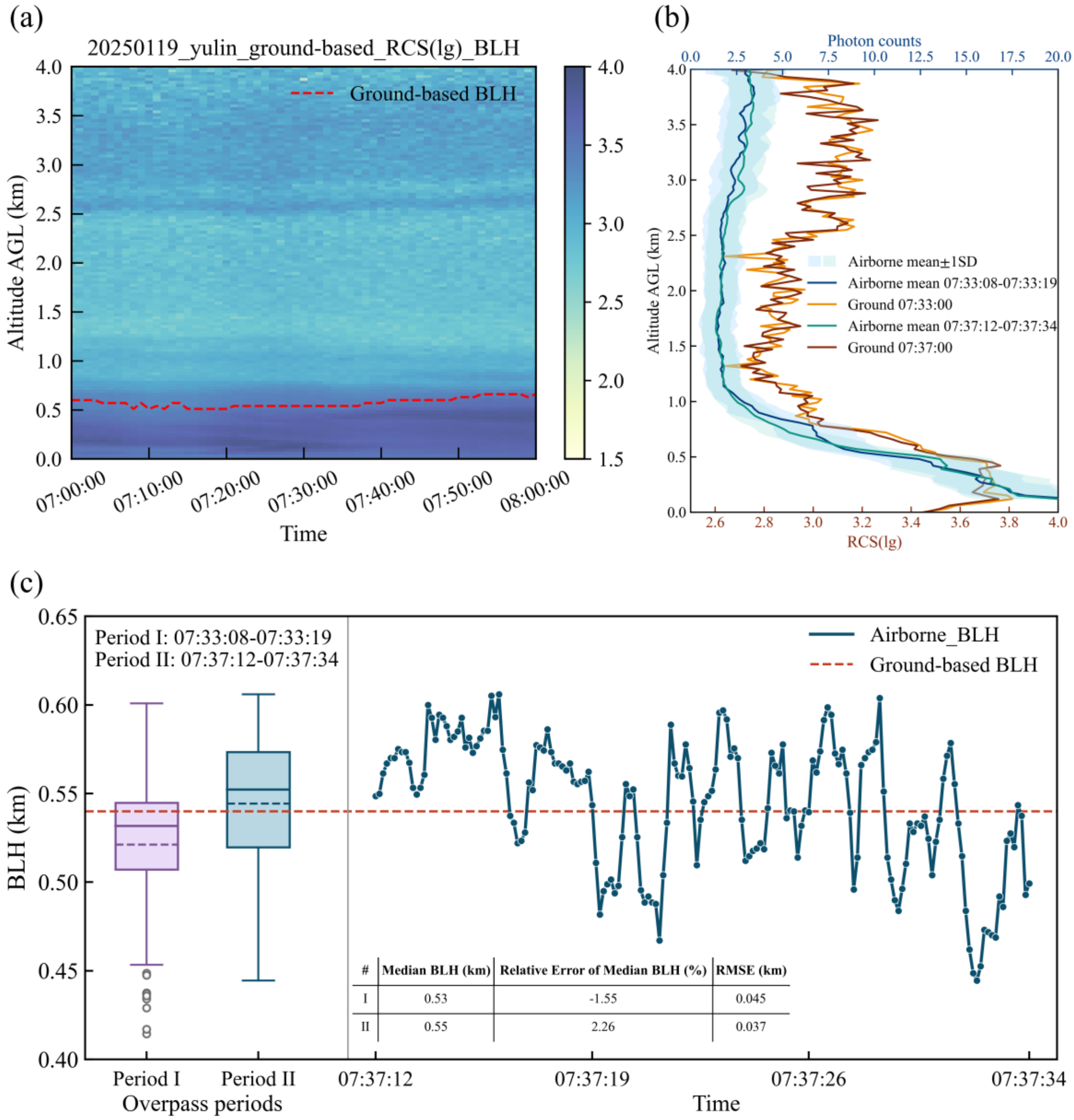

Figure 15. (a) Range-corrected signal (RCS) from the ground-based 1550 nm lidar. (b) Comparison of the backscattering signal profiles between the airborne lidar and ground-based lidar during the overpass periods. The solid lines represent the averaged airborne profiles during the overpasses, with the shaded areas indicating the standard deviation. (c) Statistical boxplots of BLH retrieved from the airborne data during two overpass periods, along with the high-temporal-resolution BLH sequence from 07:37:12 to 07:37:34 LT. The dark red horizontal dashed line indicates the reference BLH value derived from ground-based lidar signal.

The vertical structures of the averaged airborne backscattering profiles are compared with those of the ground-based lidar RCS profiles during the two overpass periods in Fig. 15b. Despite discrepancies in the absolute magnitudes of the signal intensities—arising from the distinct scattering characteristics of the 1064 nm and 1550 nm wavelengths, as well as the contrasting detection geometries (downward-pointing airborne vs. upward-pointing ground-based), the profile structures exhibit a high degree of similarity. They show excellent agreement, especially in terms of their response at the aerosol–layer interface. At an altitude of approximately 0.54 km, both types of profiles exhibit significant negative signal gradients, clearly delineating the boundary-layer top. The strong agreement between the airborne profiles during the two overpass periods also indicates that the vertical atmospheric structure remained relatively stable across the study area during the experiment. The statistical characteristics and high-frequency time sequence of the BLHs retrieved from the airborne experiment during the two overpass periods are shown in Fig. 15c. Within the 22-second window from 07:37:12 to 07:37:34 LT, the airborne system successfully acquired 176 BLH data points at a temporal resolution of 0.125 s. As illustrated in the time sequence, the retrieved BLH results exhibit high stability around the 0.54 km baseline, with fluctuations of less than 90 m. Statistical analysis further indicates that the BLHs retrieved from the airborne data during the two overpasses have negligible deviations relative to the ground-based reference. Specifically, the absolute deviation between the median airborne BLH of both periods and the ground-based BLH is merely 10 m, with a relative error of less than 2.5%, and the root-mean-square errors (RMSEs) are 45 m and 37 m, respectively. These precise quantitative error metrics robustly verify the exceptional detection performance of the airborne prototype in tracking fine-scale PBL structures with high resolution and high accuracy. The comparison in Fig. 15 also shows that the vertical position of the main aerosol gradient can be consistently identified from the 1064 and 1550 nm signals, although the two systems differ in wavelength, observation geometry, and signal magnitude. This finding indicates that the retrieved BLH is mainly determined by the vertical variation in the aerosol signal rather than its absolute intensity.

This close agreement not only demonstrates the reliability and accuracy of the airborne prototype under complex winter underlying surface conditions but also further validates the payload design philosophy proposed in this study. By synchronously acquiring high-precision surface elevation information, the airborne system can directly output the BLH relative to the actual terrain, i.e., above ground level (AGL), thereby effectively mitigating the geometric matching bias inherent in traditional detection regimes because of terrain fluctuations and errors in external digital elevation models (DEMs). This synergistic terrain–atmosphere detection capability provides important guidance for future spaceborne platforms to achieve unified and refined global BLH observations.

4.2 Complex boundary layers during summer daytime in coastal areas

Following the primary nighttime validation in Yulin, the Hainan flight experiment was used to further explore the performance of the airborne prototype under complex daytime conditions. Under the complex meteorological conditions typical of Hainan during summer—characterized by strong solar radiation, high temperatures, high humidity, and frequent cloud cover and precipitation—the boundary layer undergoes rapid spatiotemporal evolution and exhibits a highly complex vertical structure (Li et al., 2017a). This poses a severe challenge to the fine-grained near-surface detection capability of airborne lidar systems. To evaluate the detection performance of the system under these challenging conditions and identify directions for future technological improvements, three typical raw backscattering signal profiles were selected for analysis. Notably, to reduce the influence of strong background noise, the measured profiles were accumulated to a temporal resolution of 1 s.

https://doi.org/10.5194/egusphere-2026-4536
Preprint. Discussion started: 24 August 2026

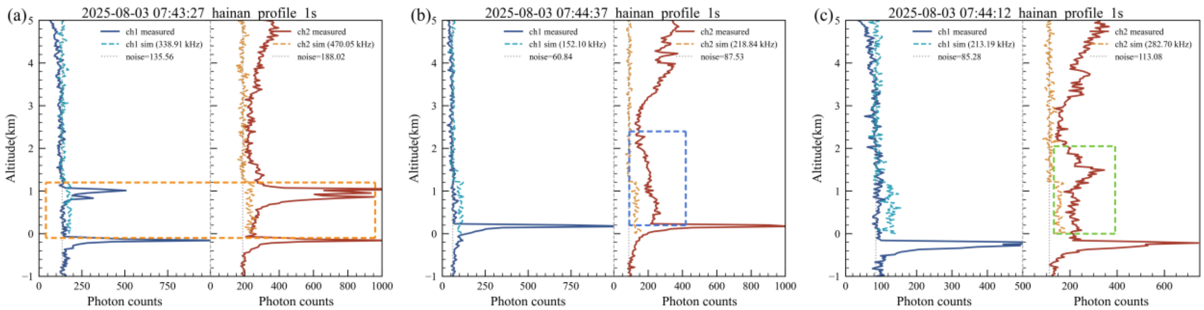

Figure 16. Typical backscattering signal profiles from the Hainan flight experiment.

As shown in Fig. 16a, at 07:43:27 LT, a cloud layer with a large optical depth was observed at an altitude of approximately 1 km (indicated by the orange box). Although part of the laser penetrated the cloud, its intensity was severely attenuated. In this case, only the hard target echo from the ground can be clearly identified, whereas the near-surface atmospheric signal did not contain sufficient information for reliable BLH retrieval. At 07:44:37 LT, corresponding to Fig. 16b, despite the laser intensity being attenuated by clouds at altitudes of 4–5 km, the near-surface aerosol signal was still effectively detected. However, owing to the impact of strong background noise, the effective atmospheric signal remained weak and its structural features were indistinct, making it difficult for the traditional wavelet transform method to reliably retrieve the BLH. The scenario in which the near-surface aerosol layer and low-level clouds overlap is shown in Fig. 16c. Although the stratification structure appeared more pronounced in this case, relying solely on the traditional wavelet transform method for BLH identification leads to considerable errors. In all three typical cases, the signal intensity in the perpendicular polarization channel (ch1) was notably weak, resulting in consistently extremely low depolarization ratios. This observation is consistent with the physical characteristics of high humidity in the Hainan region, where aerosol particles undergo hygroscopic growth and tend toward a spherical shape. This further illustrates how high-humidity environments constrain the polarization detection performance of the lidar system.

The comparison among the three profiles further shows that the factors limiting daytime BLH retrieval vary with atmospheric conditions. In Fig. 16a, the severe two-way attenuation caused by the optically thick cloud is the main limitation. Under this condition, the effective atmospheric photon counts received from below the cloud are substantially reduced, and the improvement of the BLH retrieval method alone cannot compensate for the insufficient atmospheric photon counts. In Fig. 16b, the near-surface aerosol signal remains detectable, indicating that the measured profile still contains useful information on the near-surface atmospheric structure. However, the cloud-enhanced background noise reduces the contrast of the effective atmospheric signal and weakens the gradient characteristics used for BLH identification. In Fig. 16c, the vertical stratification remains visible, but both the low-level cloud and aerosol layer produce obvious signal gradients. When the cloud-related gradient is close to or overlaps with the aerosol-related gradient, it becomes difficult for the traditional wavelet transform method to determine which gradient corresponds to the boundary layer top. In addition, the weak perpendicular polarization signal indicates that the depolarization ratio may provide limited auxiliary information for distinguishing clouds and aerosols

https://doi.org/10.5194/egusphere-2026-4536
Preprint. Discussion started: 24 August 2026

under high-humidity conditions. Therefore, dense clouds can affect daytime BLH retrieval through the combined effects of increasing the background noise, attenuating the effective atmospheric signal, and introducing ambiguity into the identification of the boundary layer top.

The results of the aforementioned analysis demonstrate that despite the complex conditions of strong background noise and frequent cloud cover during the summer daytime in coastal areas, this airborne lidar system has significant potential for near-surface atmospheric detection. The identifiable surface echoes and the near-surface aerosol signals obtained in selected cases indicate that useful atmospheric information can still be retained under daytime background-noise conditions. At the same time, these results reveal the present limitations of daytime BLH detection under dense cloud cover and clarify the directions for future system enhancements. On the hardware side, the daytime detection performance can be improved by further narrowing the filter bandwidth to reduce the solar background photons received by the system, thereby increasing the contrast between the effective atmospheric signal and the background noise. It should be noted that the 2.4 nm filter used in the Hainan experiment was selected to reproduce an approximately equivalent daytime background-noise condition and does not represent the optimum filter bandwidth for daytime detection. On the software side, profiles severely affected by cloud attenuation should first be identified through cloud screening and data-quality assessment. In addition, it is essential to develop an advanced retrieval framework to distinguish cloud-related and aerosol-related signal gradients, thereby improving the continuity and accuracy of BLH identification over long durations under complex daytime conditions (Li et al., 2017a, 2023; Roldán-Henao et al., 2024; Su et al., 2020a). However, when optically thick clouds prevent sufficient laser energy from reaching the near-surface atmosphere, or when the cloud-related gradient strongly overlaps with the aerosol-layer gradient, the loss or ambiguity of the effective atmospheric information cannot be completely resolved through retrieval-algorithm improvement alone. Therefore, reliable BLH detection under dense and complex cloud conditions remains a major challenge.

The Yulin winter nighttime experiment provided the primary validation of the airborne prototype under the expected nighttime operating conditions, whereas the additional Hainan summer daytime experiment extended the evaluation to stronger background noise and complex cloud conditions, revealing both the potential and current limitations of daytime detection. Together, the two experiments provide direct guidance for the design and operation of the future spaceborne system: under daytime conditions, the detection configuration and data-processing strategy should be adjusted according to the actual background-noise and cloud conditions, and profiles severely affected by cloud attenuation or cloud–aerosol overlap should be identified as low-quality data rather than used directly for BLH retrieval. More importantly, the theoretical simulations, scaled airborne verification, and feedback from the flight experiments together establish a closed-loop verification framework, in which the observed signal characteristics and limitations are used to guide the subsequent optimization of the spaceborne system parameters and data-processing strategy.

https://doi.org/10.5194/egusphere-2026-4536
Preprint. Discussion started: 24 August 2026

5 Conclusions

The parametric setting deviations of the PBLH in models are among the critical factors leading to forecasting errors in pollutant dispersion and various meteorological processes. Consequently, developing PBL parameterization schemes that accommodate global complexity and diversity remains an urgent challenge in terms of weather and climate prediction. The primary limitation stems from the lack of globally consistent PBLH observational data. Spaceborne lidar systems, with their distinct advantages of high detection accuracy and high spatiotemporal resolution, offer a powerful means to bridge this gap. This paper focuses on providing theoretical validation and empirical support for the parameter design of a spaceborne PBL detection lidar. On the basis of existing theories, we first modeled the spaceborne lidar system and simulated its detection performance. Following the spaceborne parameter design scheme, a scaled-down airborne lidar prototype was subsequently developed, and flight experiments were conducted in Yulin and Hainan in January and August 2025, respectively. The observational results were analyzed and compared with the theoretical simulations. This process not only demonstrates the rationality and reliability of the simulations but also validates the detection performance of the airborne prototype. Together, the simulation and experimental results provide robust support for the superior capabilities of the spaceborne lidar system and provide clear directions for its further optimization.

In summary, through systematic cross-validation between the experimental flight data analysis and theoretical simulation results, the following conclusions can be drawn:

1. Reliability of the Theoretical Model

The theoretical simulation model and flight experiments demonstrate high consistency in terms of backscattering signal profile characteristics, including background noise levels and photon count magnitude. These findings conclusively verify the physical rationality and computational accuracy of the theoretical model.

2. Superior detection performance of the scaled airborne lidar prototype

The detection performance of the scaled airborne lidar prototype was primarily validated through the Yulin winter nighttime flight experiment. The comparison results from the Yulin experiment demonstrate that under complex underlying surface conditions during the winter, the BLHs retrieved by the airborne system are highly consistent with the ground-based reference values. Specifically, the absolute deviation is constrained within 10 m, and the maximum RMSE is better than 45 m, which robustly substantiates the system's ability to capture fine-scale PBL structures. The additional Hainan summer daytime experiment showed that identifiable surface echoes and, in selected cases, near-surface aerosol signals were retained under strong background noise, high humidity, and complex cloud conditions, indicating its daytime detection potential while revealing the current limitations of BLH retrieval under such conditions. Moreover, the experiments strongly validate the “synergistic terrain–atmosphere detection” regime proposed in this study. By synchronously acquiring high-precision surface elevation information, the airborne system achieves direct output of the BLH relative to the actual terrain, thereby fundamentally eliminating the geometric matching bias inherent in traditional detection regimes caused by terrain fluctuations

https://doi.org/10.5194/egusphere-2026-4536
Preprint. Discussion started: 24 August 2026

and external DEM errors. This characteristic not only enhances detection accuracy but also provides critical technical support for future spaceborne platforms to achieve unified and refined global PBLH observations.

3. Advantages of Parameter Design for the Spaceborne PBL Detection Lidar System

Theoretically, the simulated detection accuracy of the PBLH by the spaceborne system is better than 10%, scientifically validating the parameter design from a physical perspective. Furthermore, the verified high detection accuracy of the scaled airborne prototype provides empirical support for the superiority of the spaceborne system's parameter design.

4. End-to-End Closed-Loop Verification

A closed-loop verification process has been established: starting from the spaceborne system parameter design, theoretical simulations model its operational state, and flight experiments with the scaled airborne prototype provide empirical support and refine the theoretical models, and both collectively evaluate the spaceborne system's performance and guide further parameter design optimization.

Appendix A: MODTRAN simulation results

The detailed MODTRAN simulation results corresponding to the background-radiance analysis in Sect. 2 are shown in Fig. A1. In the simulations, the satellite orbital and pointing parameters during post-deployment observation operations were used to configure the observation geometry in MODTRAN. To represent typical surface backgrounds encountered by spaceborne lidar observations, the surface albedo was varied from 0.1 to 0.6. The six panels show the simulated spectral radiance results for discrete albedo values of 0.1, 0.2, 0.3, 0.4, 0.5, and 0.6, respectively. These results provide the basis for extracting the 1064 nm band radiance used in the main text.

https://doi.org/10.5194/egusphere-2026-4536
Preprint. Discussion started: 24 August 2026

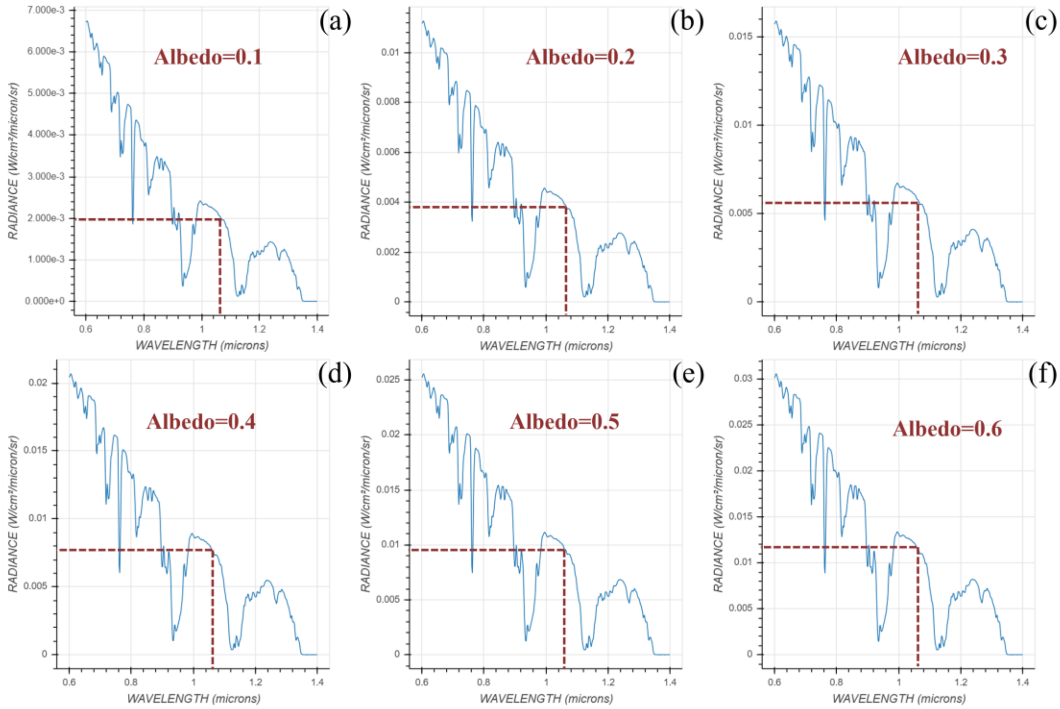

Figure A1. Radiance results simulated by MODTRAN at varying albedo values: (a) Albedo=0.1, (b) Albedo=0.2, (c) Albedo=0.3, (d) Albedo=0.4, (e) Albedo=0.5, (f) Albedo=0.6

Appendix B: MERSI-LL channel information and seasonal data distributions

The MERSI-LL channel information and the distributions of the selected FY-3E/MERSI-LL Channel 1 observations are provided in this appendix to support the background-noise evaluation described in Sect. 2. As shown in Table B1, MERSI-LL includes one low-light channel and six thermal infrared channels. Channel 1 has a central wavelength of 0.7 μm and a bandwidth of 400 nm, and was used in this study to characterize the observed background radiation level. To represent seasonal variations in the observed background radiation, one day of observational data was selected from each season. The distributions of the original radiation values observed by MERSI-LL Channel 1 on 1 January, 1 April, 1 July, and 1 October 2023 are shown in Fig. B1.

Table B1. MERSI-LL observation channel

#	Central wavelength (μm)	Bandwidth (nm)	Spatial resolution (m)
1	0.7	400	1000
2	3.8	180	1000
3	4.05	155	1000

https://doi.org/10.5194/egusphere-2026-4536
Preprint. Discussion started: 24 August 2026

4	7.2	500	1000
5	8.55	300	1000
6	10.8	1000	250
7	12.0	1000	250

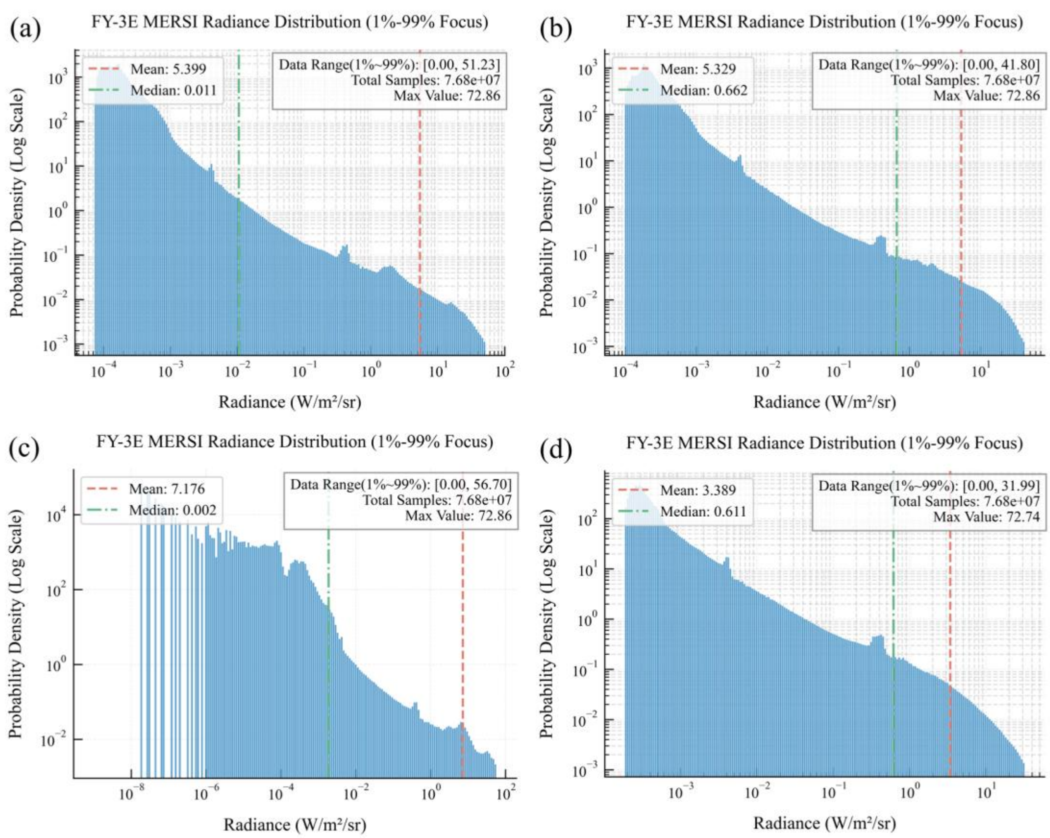

Figure B1. Distributions of radiation values observed by MERSI-LL Channel 1 on (a) 1 January, (b) 1 April, (c) 1 July, and (d) 1 October 2023.

Code and data availability

The data and code used in this study are available from the corresponding author upon reasonable request. Publicly available satellite data used in this study are cited in the text. The processed data required to reproduce the main figures will be made available through a public repository upon publication.

https://doi.org/10.5194/egusphere-2026-4536
Preprint. Discussion started: 24 August 2026

Author contributions

KM carried out the theoretical simulations, participated in the airborne experiments, performed the main data analysis, interpreted the results, and wrote the original manuscript. CW and WK contributed equally as corresponding authors. CW provided guidance on the analysis of the experimental results and revised the manuscript. WK was responsible for the lidar system parameter design and revised the manuscript. XX and GH supervised the overall experimental design and implementation and contributed to manuscript revision. RX, WL, and CL participated in the airborne experiments and contributed to the operation and testing of the airborne lidar system. YL, RZ, MJ, and XS participated in the airborne experiments and contributed to the operation of the ground-based 1550 nm lidar. All authors discussed the results and contributed to the final manuscript.

Competing interests

The authors declare that they have no conflict of interest.

Acknowledgements

Xianghui Xue is grateful for the support from the New Cornerstone Science Foundation through the XPLORER PRIZE. The authors acknowledge the use of ionospheric fitted basic parameters of Triple-Station Incoherent Scattering Radar from the Chinese Meridian Project (DOI:10.12176/01.06.00065-V01) and the MODTRAN radiative transfer simulation software. The authors thank the FY-3E satellite team for their support and the Aerosol and Carbon Detection Lidar (ACDL) payload team of the DQ-1 satellite for providing the relevant ACDL/DQ-1 data used in this study.

Financial support

This study has been supported by the open research fund of the China Meteorological Administration Xiong'an Atmospheric Boundary Layer Key Laboratory (grant no. 2023LABL-B05), the National Natural Science Foundation of China (grant nos.42125402, 42304165), and the Innovation Program for Quantum Science and Technology (grant no.2021ZD0300300).

References

Acharya, P. K., Berk, A., Anderson, G. P., Anderson, G. P., Larsen, N. F., Tsay, S. C., and Stamnes, K. H.: MODTRAN4: multiple scattering and bidirectional reflectance distribution function (BRDF) upgrades to MODTRAN, in: Optical Spectroscopic Techniques and Instrumentation for Atmospheric and Space Research III, Optical Spectroscopic Techniques and Instrumentation for Atmospheric and Space Research III, 354, https://doi.org/10.1117/12.366389, 1999.

https://doi.org/10.5194/egusphere-2026-4536
Preprint. Discussion started: 24 August 2026

Berk, A., Bernstein, L. S., Anderson, G. P., Acharya, P. K., Robertson, D. C., Chetwynd, J. H., and Adler-Golden, S. M.: MODTRAN Cloud and Multiple Scattering Upgrades with Application to AVIRIS, Remote Sensing of Environment, 65, 367–375, https://doi.org/10.1016/S0034-4257(98)00045-5, 1998.

Berk, A., Anderson, G. P., Acharya, P. K., Bernstein, L. S., Muratov, L., Lee, J., Fox, M. J., Adler-Golden, S. M., Chetwynd, J. H., Hoke, M. L., Lockwood, R. B., Cooley, T. W., and Gardner, J. A.: MODTRAN5: a reformulated atmospheric band model with auxiliary species and practical multiple scattering options, in: Multispectral and Hyperspectral Remote Sensing Instruments and Applications II, Multispectral and Hyperspectral Remote Sensing Instruments and Applications II, 88, https://doi.org/10.1117/12.578758, 2005.

Berkoff, T., Welton, E., Campbell, J., and Spinhirne, J.: The micro-pulse lidar network (MPLNET), in: Frontiers in Optics (2003), paper MK2, Frontiers in Optics, MK2, https://doi.org/10.1364/FIO.2003.MK2, 2003.

Brooks, I. M.: Finding Boundary Layer Top: Application of a Wavelet Covariance Transform to Lidar Backscatter Profiles, Journal of Atmospheric and Oceanic Technology, 20, 1092–1105, https://doi.org/10.1175/1520-0426(2003)020%3C1092:FBLTAO%3E2.0.CO;2, 2003.

Burton, S. P., Ferrare, R. A., Hostetler, C. A., Hair, J. W., Rogers, R. R., Obland, M. D., Butler, C. F., Cook, A. L., Harper, D. B., and Froyd, K. D.: Aerosol classification using airborne High Spectral Resolution Lidar measurements – methodology and examples, Atmospheric Measurement Techniques, 5, 73–98, https://doi.org/10.5194/amt-5-73-2012, 2012.

Cairo, F., Di Liberto, L., Dionisi, D., and Snels, M.: Understanding Aerosol–Cloud Interactions through Lidar Techniques: A Review, Remote Sensing, 16, 2788, https://doi.org/10.3390/rs16152788, 2024.

do Carmo, J. P., de Villele, G., Wallace, K., Lefebvre, A., Ghose, K., Kanitz, T., Chassat, F., Corselle, B., Belhadj, T., and Bravetti, P.: ATmospheric LIDar (ATLID): Pre-Launch Testing and Calibration of the European Space Agency Instrument That Will Measure Aerosols and Thin Clouds in the Atmosphere, Atmosphere, 12, 76, https://doi.org/10.3390/atmos12010076, 2021.

Comerón, A., Muñoz-Porcar, C., Rocadenbosch, F., Rodríguez-Gómez, A., and Sicard, M.: Current Research in Lidar Technology Used for the Remote Sensing of Atmospheric Aerosols, Sensors (Basel), 17, 1450, https://doi.org/10.3390/s17061450, 2017.

Degnan, J. J.: Photon-counting multikilohertz microlaser altimeters for airborne and spaceborne topographic measurements, Journal of Geodynamics, 34, 503–549, https://doi.org/10.1016/S0264-3707(02)00045-5, 2002.

Donovan, D. P., van Zadelhoff, G.-J., and Wang, P.: The EarthCARE lidar cloud and aerosol profile processor (A-PRO): the A-AER, A-EBD, A-TC, and A-ICE products, Atmospheric Measurement Techniques, 17, 5301–5340, https://doi.org/10.5194/amt-17-5301-2024, 2024.

Esselborn, M., Wirth, M., Fix, A., Weinzierl, B., Rasp, K., Tesche, M., and Petzold, A.: Spatial distribution and optical properties of Saharan dust observed by airborne high spectral resolution lidar during SAMUM 2006, Tellus B, 61, 131–143, https://doi.org/10.1111/j.1600-0889.2008.00394.x, 2009.

Fernald, F. G.: Analysis of atmospheric lidar observations: some comments, Appl. Opt., AO, 23, 652–653, https://doi.org/10.1364/AO.23.000652, 1984.

Gao, F., Schaaf, C. B., Strahler, A. H., Roesch, A., Lucht, W., and Dickinson, R.: MODIS bidirectional reflectance distribution function and albedo Climate Modeling Grid products and the variability of albedo for major global vegetation types, J. Geophys. Res., 110, D01104, https://doi.org/10.1029/2004JD005190, 2005.

Gao, L., Yan, P., Mao, J., Zhang, X., Zhang, X., Wu, Y., Jing, J., Xu, J., Deng, X., and Chi, W.: Ambient Atmospheric Aerosol Extinction Coefficient Reconstruction from PM2.5 Mass Concentrations and Application to Haze Identification in China, Aerosol Air Qual. Res., 21, 200386, https://doi.org/10.4209/aaqr.200386, 2021.

Groß, S., Esselborn, M., Weinzierl, B., Wirth, M., Fix, A., and Petzold, A.: Aerosol classification by airborne high spectral resolution lidar observations, Atmospheric Chemistry and Physics, 13, 2487–2505, https://doi.org/10.5194/acp-13-2487-2013, 2013.

Hair, J. W., Hostetler, C. A., Cook, A. L., Harper, D. B., Ferrare, R. A., Mack, T. L., Welch, W., Izquierdo, L. R., and Hovis, F. E.: Airborne High Spectral Resolution Lidar for profiling aerosol optical properties, Appl. Opt., AO, 47, 6734–6752, https://doi.org/10.1364/AO.47.006734, 2008.

Huang, R.-J., Zhang, Y., Bozzetti, C., Ho, K.-F., Cao, J.-J., Han, Y., Daellenbach, K. R., Slowik, J. G., Platt, S. M., Canonaco, F., Zotter, P., Wolf, R., Pieber, S. M., Bruns, E. A., Crippa, M., Ciarelli, G., Piazzalunga, A., Schwikowski, M., Abbaszade, G., Schnelle-Kreis, J., Zimmermann, R., An, Z., Szidat, S., Baltensperger, U., Haddad, I. E., and Prévôt, A. S. H.: High secondary aerosol contribution to particulate pollution during haze events in China, Nature, 514, 218–222, https://doi.org/10.1038/nature13774, 2014.

Jin, Y., Schaaf, C. B., Woodcock, C. E., Gao, F., Li, X., Strahler, A. H., Lucht, W., and Liang, S.: Consistency of MODIS surface bidirectional reflectance distribution function and albedo retrievals: 2. Validation, J. Geophys. Res., 108, 4159, https://doi.org/10.1029/2002JD002804, 2003.

Ke, J., Sun, Y., Dong, C., Zhang, X., Wang, Z., Lyu, L., Zhu, W., Ansmann, A., Su, L., Bu, L., Xiao, D., Wang, S., Chen, S., Liu, J., Chen, W., and Liu, D.: Development of China's first space-borne aerosol-cloud high-spectral-resolution lidar: retrieval algorithm and airborne demonstration, PhotoniX, 3, 17, https://doi.org/10.1186/s43074-022-00063-3, 2022.

Li, H., Yang, Y., Hu, X.-M., Huang, Z., Wang, G., and Zhang, B.: Application of Convective Condensation Level Limiter in Convective Boundary Layer Height Retrieval Based on Lidar Data, Atmosphere, 8, 79, https://doi.org/10.3390/atmos8040079, 2017a.

Li, H., Yang, Y., Hu, X., Huang, Z., Wang, G., Zhang, B., and Zhang, T.: Evaluation of retrieval methods of daytime convective boundary layer height based on lidar data, JGR Atmospheres, 122, 4578–4593, https://doi.org/10.1002/2016JD025620, 2017b.

Li, H., Liu, B., Ma, X., Ma, Y., Jin, S., Fan, R., Wang, W., Fang, J., Zhao, Y., and Gong, W.: The Influence of Temperature Inversion on the Vertical Distribution of Aerosols, Remote Sensing, 14, 4428, https://doi.org/10.3390/rs14184428, 2022a.

Li, H., Liu, B., Ma, X., Jin, S., Wang, W., Fan, R., Ma, Y., Wei, R., and Gong, W.: Estimation of Planetary Boundary Layer Height From Lidar by Combining Gradient Method and Machine Learning Algorithms, IEEE Trans. Geosci. Remote Sensing, 61, 1–11, https://doi.org/10.1109/TGRS.2023.3329122, 2023.

Li, Y. D., Wang, C., Xue, X. H., Wang, Y., Shang, X., Jia, M. J., and Chen, T. D.: Study on the Parameters of Ice Clouds Based on 1.5 μm Micropulse Polarization Lidar, Remote Sensing, 14, 5162, https://doi.org/10.3390/rs14205162, 2022b.

Liu, B., Ma, X., Ma, Y., Li, H., Jin, S., Fan, R., and Gong, W.: The relationship between atmospheric boundary layer and temperature inversion layer and their aerosol capture capabilities, Atmospheric Research, 271, 106121, https://doi.org/10.1016/j.atmosres.2022.106121, 2022.

Liu, J., Huang, J., Chen, B., Zhou, T., Yan, H., Jin, H., Huang, Z., and Zhang, B.: Comparisons of PBL heights derived from CALIPSO and ECMWF reanalysis data over China, Journal of Quantitative Spectroscopy and Radiative Transfer, 153, 102–112, https://doi.org/10.1016/j.jqsrt.2014.10.011, 2015.

Liu, Z., Mortier, A., Li, Z., Hou, W., Goloub, P., Lv, Y., Chen, X., Li, D., Li, K., and Xie, Y.: Improving Daytime Planetary Boundary Layer Height Determination from CALIOP: Validation Based on Ground-Based Lidar Station, Advances in Meteorology, 2017, 1–14, https://doi.org/10.1155/2017/5759074, 2017.

Marais, W. J., Holz, R. E., Hu, Y. H., Kuehn, R. E., Eloranta, E. E., and Willett, R. M.: Approach to simultaneously denoise and invert backscatter and extinction from photon-limited atmospheric lidar observations, Appl. Opt., AO, 55, 8316–8334, https://doi.org/10.1364/AO.55.008316, 2016.

Mason, S. L., Barker, H. W., Cole, J. N. S., Docter, N., Donovan, D. P., Hogan, R. J., Hünerbein, A., Kollias, P., Puigdomènech Treserras, B., Qu, Z., Wandinger, U., and van Zadelhoff, G.-J.: An intercomparison of EarthCARE cloud, aerosol, and precipitation retrieval products, Atmospheric Measurement Techniques, 17, 875–898, https://doi.org/10.5194/amt-17-875-2024, 2024.

Measures, R. M.: Laser Remote Sensing: Fundamentals and Applications, Wiley, New York, 1984.

Ming, K., Wang, C., Xue, X., Wu, J., and Chen, T.: Parameter optimization for Rayleigh–Mie lidar under different dust conditions for the landing area of Martian Tianwen-1, Earth and Planetary Physics, 8, 899–909, https://doi.org/10.26464/epp2024061, 2024.

Paffrath, U., Lemmerz, C., Reitebuch, O., Witschas, B., Nikolaus, I., and Freudenthaler, V.: The Airborne Demonstrator for the Direct-Detection Doppler Wind Lidar ALADIN on ADM-Aeolus. Part II: Simulations and Rayleigh Receiver Radiometric Performance, Journal of Atmospheric and Oceanic Technology, 26, 2516–2530, https://doi.org/10.1175/2009JTECHA1314.1, 2009.

Palm, S. P., Selmer, P., Yorks, J., Nicholls, S., and Nowottnick, E.: Planetary Boundary Layer Height Estimates From ICESat-2 and CATS Backscatter Measurements, Front. Remote Sens., 2, 716951, https://doi.org/10.3389/frsen.2021.716951, 2021.

Pappalardo, G., Amodeo, A., Apituley, A., Comeron, A., Freudenthaler, V., Linné, H., Ansmann, A., Bösenberg, J., D'Amico, G., Mattis, I., Mona, L., Wandinger, U., Amiridis, V., Alados-Arboledas, L., Nicolae, D., and Wiegner, M.: EARLINET:

https://doi.org/10.5194/egusphere-2026-4536
Preprint. Discussion started: 24 August 2026

towards an advanced sustainable European aerosol lidar network, Atmospheric Measurement Techniques, 7, 2389–2409, https://doi.org/10.5194/amt-7-2389-2014, 2014.

Pauly, R. M., Yorks, J. E., Hlavka, D. L., McGill, M. J., Amiridis, V., Palm, S. P., Rodier, S. D., Vaughan, M. A., Selmer, P. A., Kupchock, A. W., Baars, H., and Gialitaki, A.: Cloud-Aerosol Transport System (CATS) 1064 nm calibration and validation, Atmospheric Measurement Techniques, 12, 6241–6258, https://doi.org/10.5194/amt-12-6241-2019, 2019.

Prasad, P., Basha, G., and Ratnam, M. V.: Is the atmospheric boundary layer altitude or the strong thermal inversions that control the vertical extent of aerosols?, Science of The Total Environment, 802, 149758, https://doi.org/10.1016/j.scitotenv.2021.149758, 2022.

Reitebuch, O., Lemmerz, C., Nagel, E., Paffrath, U., Durand, Y., Endemann, M., Fabre, F., and Chaloupy, M.: The Airborne Demonstrator for the Direct-Detection Doppler Wind Lidar ALADIN on ADM-Aeolus. Part I: Instrument Design and Comparison to Satellite Instrument, Journal of Atmospheric and Oceanic Technology, 26, 2501–2515, https://doi.org/10.1175/2009JTECHA1309.1, 2009.

Roldán-Henao, N., Yorks, J. E., Su, T., Selmer, P. A., and Li, Z.: Statistically Resolved Planetary Boundary Layer Height Diurnal Variability Using Spaceborne Lidar Data, Remote Sensing, 16, 3252, https://doi.org/10.3390/rs16173252, 2024.

Sawamura, P., Moore, R. H., Burton, S. P., Chemyakin, E., Müller, D., Kolgotin, A., Ferrare, R. A., Hostetler, C. A., Ziemba, L. D., Beyersdorf, A. J., and Anderson, B. E.: HSRL-2 aerosol optical measurements and microphysical retrievals vs. airborne in situ measurements during DISCOVER-AQ 2013: an intercomparison study, Atmospheric Chemistry and Physics, 17, 7229–7243, https://doi.org/10.5194/acp-17-7229-2017, 2017.

Shao, Y., Wang, J., Hu, X., Yang, Y., Miao, P., Chen, X., Li, J., Deng, S., Li, Y., and Li, H.: System Design and Technical Characteristics of Fengyun-3E Meteorological Satellite, Adv. Astronaut. Sci. Technol., 5, 363–374, https://doi.org/10.1007/s42423-022-00128-2, 2022.

Su, T. and Zhang, Y.: Deep-learning-derived planetary boundary layer height from conventional meteorological measurements, Atmospheric Chemistry and Physics, 24, 6477–6493, https://doi.org/10.5194/acp-24-6477-2024, 2024.

Su, T., Li, Z., and Kahn, R.: A new method to retrieve the diurnal variability of planetary boundary layer height from lidar under different thermodynamic stability conditions, Remote Sensing of Environment, 237, 111519, https://doi.org/10.1016/j.rse.2019.111519, 2020a.

Su, T., Li, Z., Li, C., Li, J., Han, W., Shen, C., Tan, W., Wei, J., and Guo, J.: The significant impact of aerosol vertical structure on lower atmosphere stability and its critical role in aerosol–planetary boundary layer (PBL) interactions, Atmospheric Chemistry and Physics, 20, 3713–3724, https://doi.org/10.5194/acp-20-3713-2020, 2020b.

Sugimoto, N., Nishizawa, T., Shimizu, A., and Jin, Y.: The Asian Dust and Aerosol Lidar Observation Network (AD-Net), in: Light, Energy and the Environment (2016), paper EW2A.1, Optics and Photonics for Energy and the Environment, EW2A.1, https://doi.org/10.1364/EE.2016.EW2A.1, 2016.

Tang, Y., Han, S., Yao, Q., Cai, Z., Qiu, Y., and Feng, J.: Analysis of a Severe Regional Haze-fog-dust Episode over North China in Autumn by Using Multiple Observation Data, Aerosol Air Qual. Res., 20, 2211–2225, https://doi.org/10.4209/aaqr.2019.11.0567, 2020.

Tao, M., Gui, L., Li, R., Wang, L., Liang, S., Li, Q., Wang, L., Yu, C., and Chen, L.: Tracking prevailing dust aerosol over the air pollution in central China with integrated satellite and ground observations, Atmospheric Environment, 253, 118369, https://doi.org/10.1016/j.atmosenv.2021.118369, 2021.

Wang, C., Jia, M., Xia, H., Wu, Y., Wei, T., Shang, X., Yang, C., Xue, X., and Dou, X.: Relationship analysis of $PM_{2.5}$ and boundary layer height using an aerosol and turbulence detection lidar, Atmos. Meas. Tech., 12, 3303–3315, https://doi.org/10.5194/amt-12-3303-2019, 2019.

Wang, R., Zhang, Q., Yue, P., Huang, Q., Zeng, J., and Chou, Y.: Characteristics of boundary layer height and its influencing factors in global monsoon regions, Global and Planetary Change, 231, 104309, https://doi.org/10.1016/j.gloplacha.2023.104309, 2023.

Wehr, T., Kubota, T., Tzeremes, G., Wallace, K., Nakatsuka, H., Ohno, Y., Koopman, R., Rusli, S., Kikuchi, M., Eisinger, M., Tanaka, T., Taga, M., Deghaye, P., Tomita, E., and Bernaerts, D.: The EarthCARE mission – science and system overview, Atmospheric Measurement Techniques, 16, 3581–3608, https://doi.org/10.5194/amt-16-3581-2023, 2023.

Weitkamp, C. (Ed.): Lidar: Range-Resolved Optical Remote Sensing of the Atmosphere, Springer, New York, https://doi.org/10.1007/b106786, 2005.

Welton, E. J., Campbell, J. R., Lewis, J. R., Lolli, S., Stewart, S. A., Belcher, L. R., Holben, B. N., Giles, D. M., and Slutsker, I.: The NASA Micro Pulse Lidar Network (MPLNET): Early Results from Development of Diurnal Climatologies, in: 2021 IEEE International Geoscience and Remote Sensing Symposium IGARSS, 2021 IEEE International Geoscience and Remote Sensing Symposium IGARSS, ISSN: 2153-7003, 1432–1433, https://doi.org/10.1109/IGARSS47720.2021.9553788, 2021.

Wen, E., Li, L., Hu, X., Xu, H., Gu, H., Zhu, J., and Li, Z.: On-orbit radiometric calibration of FY-3E MERSI-LL low light band (LLB) using the Moon, Opt. Express, OE, 33, 9674–9694, https://doi.org/10.1364/OE.551275, 2025.

Yu, T., Chen, L., Xu, N., Xu, H., Hu, X., and Zhang, X.: Fengyun-3E Low Light Observation and Nighttime Lights Product, IEEE Transactions on Geoscience and Remote Sensing, 61, 1–12, https://doi.org/10.1109/TGRS.2023.3292236, 2023.

Zhang, P., Hu, X., Sun, L., Xu, N., Chen, L., Zhu, A., Lin, M., Lu, Q., Yang, Z., Yang, J., and Wang, J.: The On-Orbit Performance of FY-3E in an Early Morning Orbit, Bulletin of the American Meteorological Society, 105, E144–E175, https://doi.org/10.1175/BAMS-D-22-0045.1, 2024.

Zhang, W., Guo, J., Miao, Y., Liu, H., Zhang, Y., Li, Z., and Zhai, P.: Planetary boundary layer height from CALIOP compared to radiosonde overChina, Atmos. Chem. Phys., 16, 9951–9963, https://doi.org/10.5194/acp-16-9951-2016, 2016.